CONTROL SYSTEM DESIGN OF ACTIVE PRIMARY MIRROR FOR THE ADVANCED LIDAR CONCEPT SATELLITE

Mauro Manetti, Marco Morandini and Paolo Mantegazza

Dipartimento di Ingegneria Aerospaziale
Politecnico di Milano

Giugno 2007

North East South West
INTERREG IIIC
PROJECT PART-FINANCED BY THE EUROPEAN UNION
MATEO

Contents

List of Figures

List of Tables

1 Introduction

The human knowledge of the universe is strongly based on telescopes observations. The main advantage of a space telescope is linked to the absence of atmospheric turbulence, which distorts astronomical images. The disadvantage is the need of keeping telescope dimensions within reasonable sizes, to ease their orbital displacement, with a consequent limit on images resolution.

In recent years different projects for space telescopes have been developed and realized, the most famous one for astronomical observations being the Hubble Space Telescope. The quest for the highest image resolution possible is now pushing toward larger and larger telescopes. As said such a requirement conflicts with large telescopes in outer earth space because of the problem of putting them into orbit. So from this point of view ground telescopes represent a more viable solution, but the problems linked to atmospheric turbulence distortion and manufacturing errors on very large mirrors risk to dispel all the theoretical advantages. These have been the main reasons for the development of different adaptive mirror technologies. The adaption idea is to modify the mirror shape to correct both the image distortion caused by atmospheric turbulence and any possible geometric error related to the mirror construction. These techniques have been already applied to some ground telescopes with successful improvements of image qualities.

Adaptive concepts can be useful for space based telescope also because, if it is true that there is no atmosphere distortion, there are nonetheless important problems related to thermoelastic deformations of the mirror and of the satellite structure, interaction with the attitude control system and the always present problem of geometric imprecision in the telescope construction and mounting in space. The latest projects trying to develop space telescopes with wider mirrors than the past ones will be all affected by manufacturing errors, deployment imprecision and thermoelastic deformations that might compromise telescope performances anyhow. So the need arises of applying adaptive concepts in space too. Space telescopes with active primary mirrors technology do not exist right now, the most advanced project being the James Webb Space Telescope. It uses a segmented mirror technology which impedes to deform the mirror surface with continuity, thus leading to somewhat inferior performances compared to continuous mirrors.

The aim of this report is to show the preliminary design and simulation of a possible adaptive control system related to the primary mirrors of the LIDAR telescope satellite. The LIDAR primary mirror is built with seven independent continuous mirrors, as shown in figure 1; the position and continuous deformations of each of these mirrors can be controlled using a number of dedicated, colocated sensor-actuator pairs. Using seven continuously deformable mirrors allows to correct deployment errors, manufacturing errors, thermal and other environmental disturbances; at the same time, the telescope structure could be significantly lighter than that of a segmented telescope with rigid mirrors. The control approach is derived from experiences gathered in relation to, field proven, adaptive secondary mirror technologies for ground telescopes. The related design is based on a deformable primary mirror assuring surface continuity with the consequent possibility of obtaining continuous wavy mirror shapes. To this end the design is based on a large number of discrete controllers using collocated Capacitive Sensors and Voice Coil Motor Actuators. The control system is implemented in a fully decentralized way, thus limiting the exchange of information between 186 discrete actuation points. It is based on a fairly simple control law based on an appropriate feedforward and a simple local PD2 feedback, applied independently at every control unit. This report presents the basic satellite model characterization, focuses on the actuators models and shows the final modal reduction of the dynamic system. It then reports the main control law properties and their parameters setting. Simulations results are reported eventually, to show the different parameters affecting control performances and evaluating the achievement of

the required controller specifications. Possible negative interactions between the satellite attitude control system and the active mirrors controllers are also taken into account.

2 Satellite description

The Nastran Finite Element Model of the LIDAR telescope satellite has been provided by "Carlo Gavazzi Space". This section does aim neither at developing the satellite components nor their finite element model, but gives only an overview of the satellite main features needed to understand all the facets related to the mirrors control system design.

Figure 1(a) presents a sketch showing all of the main satellite parts, while figure 1(b) shows the finite element model used to perform the simulations.

The baffle has to be asymmetric to assure that the sunlight does not penetrate the optical tube. Its deployment will be based on an inflatable technology needing a pressurized gas only for the first phase, because the structure will eventually be stiff enough to be self standing after its opening. The designed baffle is a truss structure that has been modeled using beam elements to reproduce the structure stiffness after the deployment. The baffle foils are modeled as non-structural masses on trusses, to correctly contribute to the main vibration modes of the model.

The satellite has two main solar power units connected at the bottom of the satellite central body. The solar panels are described by shell elements connected to each other by beam elements that simulate the deployment hinges.

The satellite central body can be divided into two main parts. The lower one is the bus containing all of the satellite equipments. The bus is modeled through shell elements simulating its walls and beam elements simulating the frame structure. Equipments dummies are described by means of solid elements connected to the bus panels. The upper satellite body represents the payload repository and is modeled in the same way as the bus.

As shown in figure 2(a) the telescope primary mirror surface has a 4 m diameter and it is divided in 7 sectors: a central element and six petals placed around it. Each petal has 25 actuators placed uniformly on its surface, while the central mirror has 36 actuators. All mirrors are made with a 1 mm thick zerodur material, modeled using plate elements. The back-plane design guarantees a sufficiently rigid support for the mirror and must have a low thermal deformation, comparable to zerodur glass. In the work here presented we have always used the first project solution based on sandwich panels with two laminate skins and honeycomb, modeled respectively with laminated plates and solid elements. The upper composite laminate must have the same shape as the mirror, so the upper surface must be as curved as the mirror. It should be remarked that, once the satellite is in orbit, the mirror surface is constrained to the back-plane only trough the action of actuators, so without control forces every part of the primary mirror is free to move along the actuating directions. In the analysis performed up to now the actuators directions are not normal to the mirror surface but all are aligned along the satellite spin axis, thus allowing a rigid vertical piston movement of each mirror.

All the controller units are collocated voice coil motor actuators and capacitive sensors as shown in figure 2(b). The actuators mobile parts are the stingers and they are modeled by steel beam elements. The stingers are connected to the back-plane trough springs (CBUSH elements), thus allowing a stiffness that simulates the presence of axial bearings (fig.2(b)). In particular for each stinger there are two CBUSH elements, one between the stinger and the upper back-plane skin, simulating only the bearing, and one between the stinger and the lower back-plane, simulating the bearing and, possibly, the presence of the axial control force. A very low fictitious axial force is

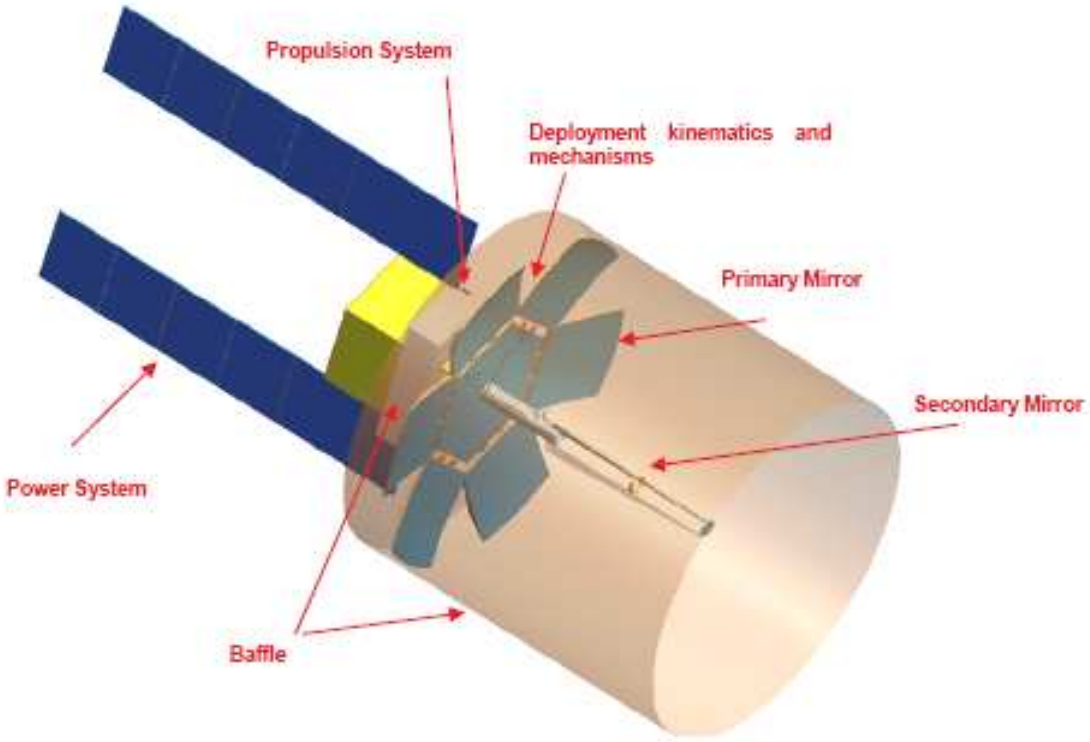

(a) Full satellite representation (Credit by Carlo Gavazzi Space).

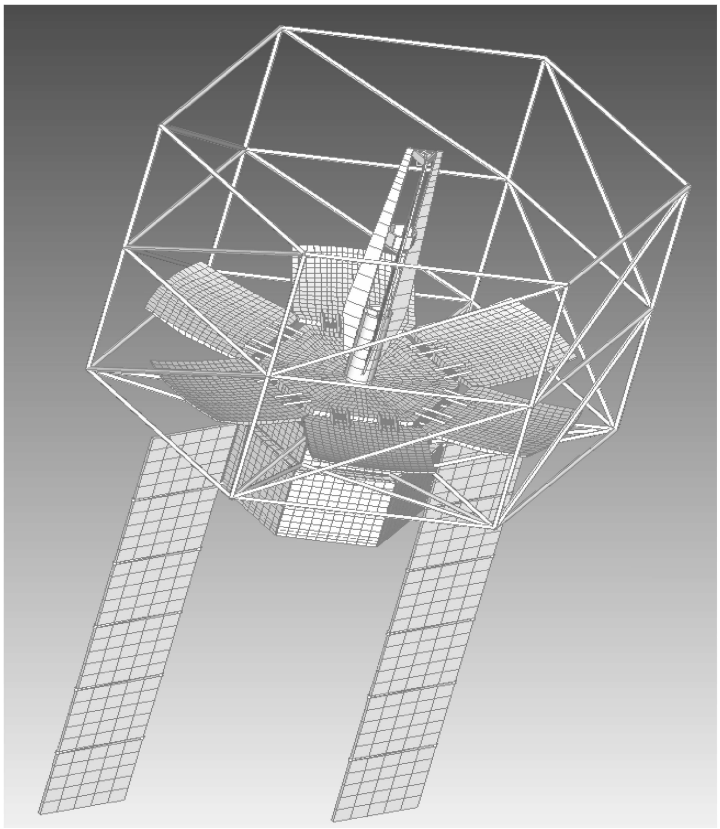

(b) Finite element model used for system simulation.

Figure 1: LIDAR satellite.

needed to remove the rigid movements between the mirrors and the back-plane as it will appear more clearly later on. The bearing transverse stiffness is supposed to be equal to 6000 [KN/m], the axial one to 1 [N/m]. The connections between the stingers and the mirror are assumed as spherical hinges because the solution of this problem is not clear yet. It is likely that some actuators connections will be realized as spherical hinges and others constrained only along the axial direction. The final solution is not obvious because the actuators have to supply the connection between the mirrors and the back-plane, but at the same time they have to allow all the mirrors rigid motions, possibly with the least thermal interaction between mirrors and back-planes. An ideal solution could be a single actuator along the satellite spin direction hinged at the center of each mirror, and all the other oriented normally to the mirrors surfaces and free to move along the mirrors plane. In this manner all rigid motions (translational and rotational) would be preserved without additional in-plane forces due to a non normal actuating action, and without thermal interaction between mirrors and back-plates. The mass (0.1 Kg) of the fixed body of each actuator is split into two parts, one linked to the upper and one to the lower back-plane skin. Finally 186 scalar points (SPOINT) were defined using 186 multipoint constraints equations (MPC). The value of the scalar points is equal to the difference between the stingers displacements and the actuators body, thus allowing to introduce the degree of freedom directly related to directions to be controlled. Moreover to verify the absence of possible negative interactions between the satellite attitude control system and the active mirrors control system, we carried out simulations with both controllers activated. Thus the model takes into account also the three free rotational degrees of freedom of the satellite so that a reasonable attitude control system has been designed and applied to evaluate the above mentioned interactions.

The six petals are constrained to the satellite main structure trough hinges. The hinges are modeled by shell and beam elements to allow the simulation of ball bearings. The material used simulates the presence of Elastic Memory Composites (EMC) that allow the petals opening once in orbit. We anticipate that the control simulations will show the deficiency of this first hinges project solution, because it doesn't guarantee a sufficient structural stiffness. Figure 3 reports one of the first six elastic modal forms, that represent a sort of rigid rotation of petals mirrors and back-planes together around the petals hinges. These modes are difficult to observe and control as they are coupled to the mirrors rigid motions, making it difficult to reach the requested control precision. Some analysis have demonstrated that to obtain good controller performances the initial modal frequencies of 6 Hz have to be augmented up to 20 Hz by stiffening the hinges, another possible solution being the use of dampers on every hinge.

The secondary mirror is mounted over a spike at a distance of about 3 meters from the primary mirror center. The spike has been modeled with shell elements, while the cylinder at the base with beam elements. The secondary mirror optics has been simulated by a concentrated mass put at the top of the spike.

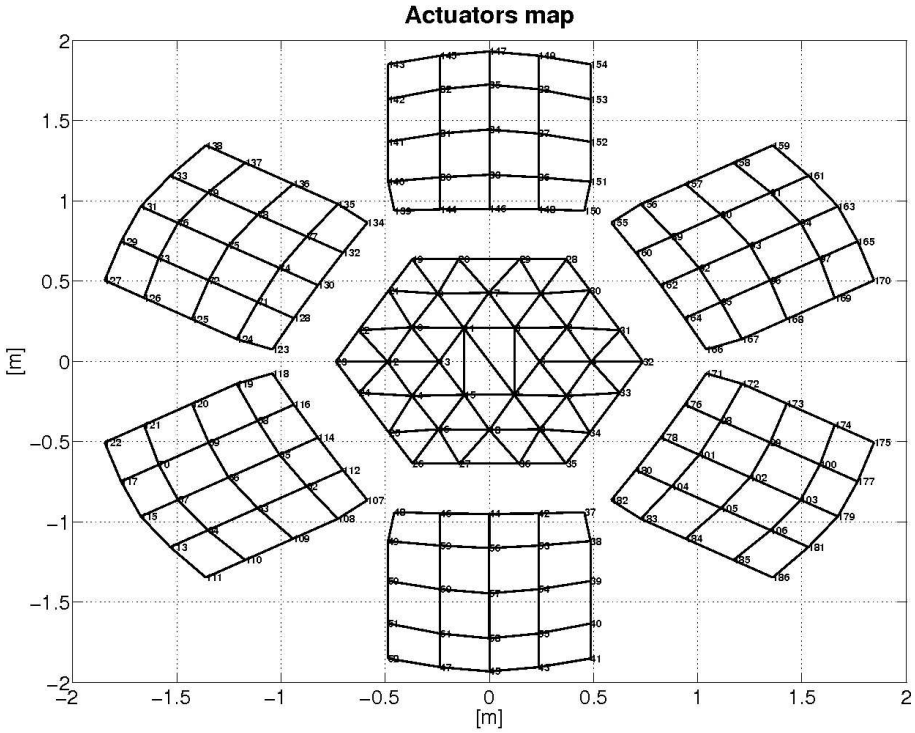

(a) Actuators map on telescope primary mirror.

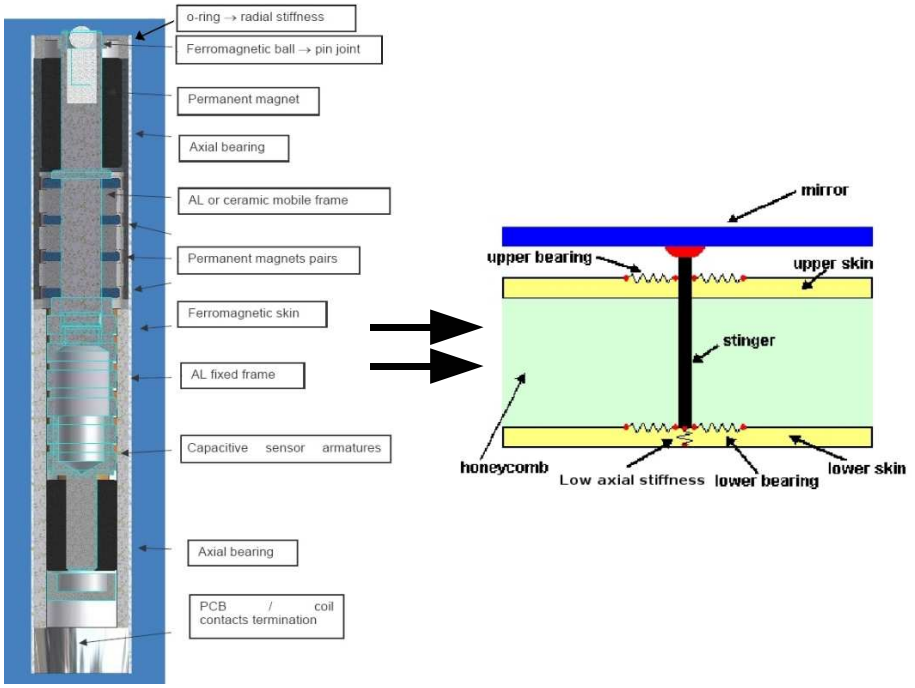

(b) Actuator model sketch (Credit by Carlo Gavazzi Space).

Figure 2: Actuator map and actuator detailed description.

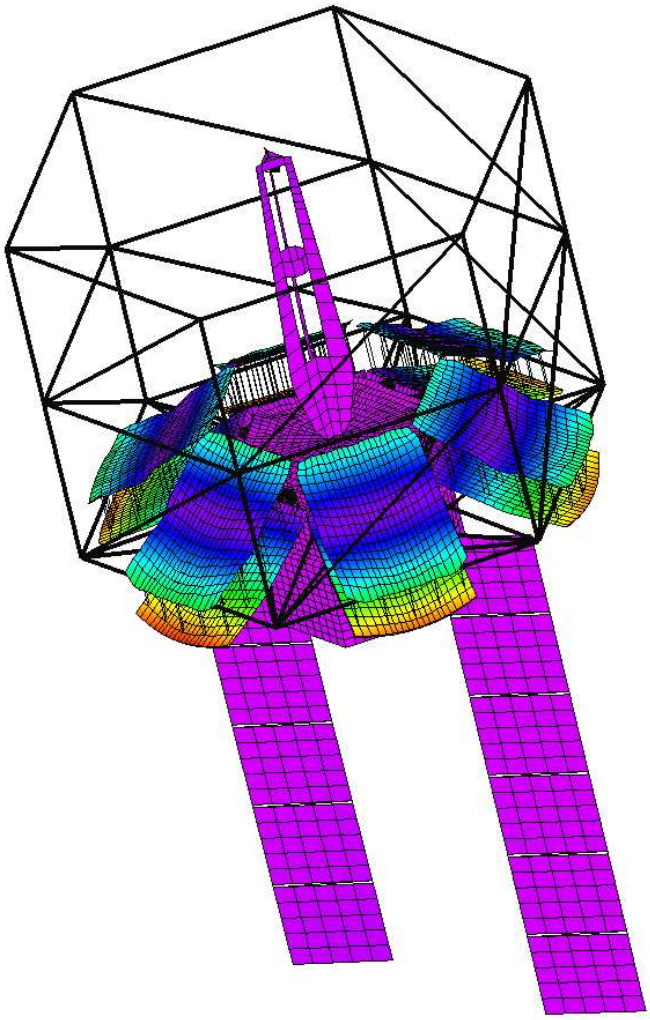

Figure 3: First petals elastic modal form.

3 Modal approach

Using the finite element model just described it is possible to characterize the satellite structural behavior and to extract all the data required for the simulation and design of the control system. The model has to be reduced because the finite element model has too many degrees of freedom, mostly useless for the design and verification of the active control system. The choice of a normal modes reduction, allows to introduce in a simple way the structural damping and to easily build the model state representation. The i^{th} modal equation can be written as:

$$\ddot{q}_i + 2\xi_i\omega_i\dot{q}_i + \omega_i^2 q = f_i^C + f_i^A + f_i^e \qquad i = 1 \dots n_m \tag{1}$$

where q_i represents the normal mode coordinate, ω_i, ξ_i, f_i^C, f_i^A, f_i^e are respectively the natural frequency, the damping coefficient, the modal active mirror control force, the modal attitude control couple and any external disturbing force, n_m is the number of modes used. The modal forces can

be written as:

$$f^C = X^T f^C \tag{2}$$
$$f^A = X^T F^A \tag{3}$$
$$f^e = X^T F^e \tag{4}$$
$$\tag{5}$$

where F^C, F^A and F^e are respectively the active mirrors control forces, the attitude control couple and the external forces on physical degrees of freedom, and X represents the $(n_a + n_{rr}) \times n_m$ mode shape matrix, evaluated at each scalar point defining a mode:

$$X = \begin{bmatrix} X_1^1 & X_1^2 & \dots & X_1^{n_m} \\ X_2^1 & X_2^2 & \dots & X_2^{n_m} \\ \vdots & \vdots & \vdots & \vdots \\ X_{n_a+n_{rr}}^1 & X_{n_a+n_{rr}}^2 & \dots & X_{n_a+n_{rr}}^{n_m} \end{bmatrix} \tag{6}$$

where n_a is the actuators number, while n_{rr} represents the 3 rotational dof of the free satellite. The scalar points S can be written as:

$$S = US_g = UX_g q \tag{7}$$

where S_g are all the FEM degrees of freedom and X_g the global modal matrix, U is the matrix that extracts and combines the displacements of interest. So we can give the following expression of condensed modal matrix:

$$X = UX_g \tag{8}$$

Now the whole state system representation can be written as:

$$\begin{Bmatrix} \dot{x}_{2_1} \\ \dot{x}_{1_1} \\ \dot{x}_{2_2} \\ \dot{x}_{1_2} \\ \vdots \\ \vdots \\ \dot{x}_{2_{n_m}} \\ \dot{x}_{1_{n_m}} \end{Bmatrix} = \begin{bmatrix} -2\xi_1\omega_1 & -\omega_1^2 & & & & & & \\ 1 & 0 & & & & & & \\ & & -2\xi_2\omega_2 & -\omega_2^2 & & & & \\ & & 1 & 0 & & & & \\ \vdots & \vdots & \vdots & \vdots & \vdots & \vdots & & \\ \vdots & \vdots & \vdots & \vdots & \vdots & \vdots & & \\ & & & & -2\xi_{n_m}\omega_{n_m} & -\omega_{n_m}^2 & & \\ & & & & 1 & 0 & & \end{bmatrix} \begin{Bmatrix} x_{2_1} \\ x_{1_1} \\ x_{2_2} \\ x_{1_2} \\ \vdots \\ \vdots \\ x_{2_{n_m}} \\ x_{1_{n_m}} \end{Bmatrix} + \begin{Bmatrix} f_1^C + f_1^A + f_1^e \\ 0 \\ f_1^C + f_1^A + f_2^e \\ 0 \\ \vdots \\ \vdots \\ f_{n_m}^C + f_{n_m}^A + f_{n_m}^e \\ 0 \end{Bmatrix} \tag{9}$$

and in a more compact form the system becomes:

$$\dot{x} = Ax + \tilde{f} \tag{10}$$

Previous studies have shown that the mirror actuators transfer functions can be approximated as first order dynamic system, so their characterization passes trough a unique time constant parameter:

$$\dot{f}^C = Df^C + af_{req}^C \tag{11}$$

where D is the scalar matrix $-aI$, f^C is the vector of real control forces applied to the mirror, f_{req}^C are control forces commanded at actuators input. The complete system can be rewritten as:

$$\begin{Bmatrix} \dot{x} \\ \dot{f}^C \end{Bmatrix} = \begin{bmatrix} A & \tilde{X}^T \\ 0 & D \end{bmatrix} \begin{Bmatrix} x \\ f^C \end{Bmatrix} + \begin{Bmatrix} \tilde{f_m^e} + \tilde{f^A} \\ af_{req}^C \end{Bmatrix} \tag{12}$$

The output S of the system are the displacements along the actuator axial axis corresponding to the collocated sensor points, and the three free rotations of the satellite:

$$\left\{ \begin{array}{c} S_1 \\ S_2 \\ \vdots \\ S_{n_a+n_{rr}} \end{array} \right\} = \left[\begin{array}{ccccc} 0 & X_1^1 & \dots & 0 & X_1^{n_m} \\ 0 & X_2^1 & \dots & 0 & X_2^{n_m} \\ \vdots & \vdots & \dots & \vdots & \vdots \\ 0 & X_{n_a+n_{rr}}^1 & \dots & 0 & X_{n_a+n_{rr}}^{n_m} \end{array} \right] \left\{ \begin{array}{c} x_{2_1} \\ x_{1_1} \\ \vdots \\ x_{2_{n_m}} \\ x_{1_{n_m}} \end{array} \right\} = \left[\tilde{X} \right] \{x\} \tag{13}$$

A transformation T can be introduced to obtain a fully uncoupled system that represents the final equations of motions:

$$\bar{x} = x + T f^C \tag{14}$$

$$T = (A + DI)^{-1} \tilde{X}^T \tag{15}$$

$$\left\{ \begin{array}{c} \dot{\bar{x}} \\ \dot{f}^C \end{array} \right\} = \left[\begin{array}{cc} A & 0 \\ 0 & D \end{array} \right] \left\{ \begin{array}{c} \bar{x} \\ f^C \end{array} \right\} + \left\{ \begin{array}{c} \tilde{f^e} + \tilde{f^A} + aT f_{req}^C \\ a f_{req}^C \end{array} \right\} \tag{16}$$

The system can be integrated using either its transition matrix or an explicit Runge-Kutta algorithms. The first method takes advantage of the uncoupled structure of the state matrix, that allow the close form determination of the needed transition matrices. This greatly reduces the computational time and simplifies the calculations. On the other hand Runge-Kutta algorithms allow a simple introduction of saturation nonlinearities or arbitrary time varying forces, but the related computation time will be higher. The control sampling time is split into two steps to consider the computational delay between the positions measurements and the new force application, as it will be shown in section 7 (fig. 4(a)). The mirrors displacements are measured by capacitive sensors, whose dynamic have been modeled with a first order approximation. So the acquired position can be expressed as:

$$\dot{p}^{mes} = -[\searrow b \swarrow] p_{mes} + bS \tag{17}$$

where S is the position obtained trough the simulation of the dynamic system and p^{mes} the measured position. Such an approximation of sensors dynamics is not introduced in the state space model directly because it could create problems in finding a simple transformation T to uncouple the state space structure, to greatly simplify the transition matrix calculation. For this reason equation 17 is implemented in the code of the controller as a filter that acts on the mirrors position measures and not as part of the overall dynamic system. In this way it is possible to have a good representation of the effect of delay and shaping linked to sensors dynamics, without compromising the system uncoupled structure previously obtained.

Moreover the simulation can take actuators Coulomb friction, due to the bearings guides, into account. This implies the possibility of inserting a constant force opposing the velocity direction. A few test of this modeling feature have demonstrated that the related effect is almost negligible in our project.

To describe the structural satellite behavior 3200 modes were chosen, covering frequencies up to 1000 Hz. In general the number of modes must guarantee a good model reduction from a dynamical point of view and the presence of a sufficient number of primary mirror modes to correctly represent complex mirror shapes, at least at the points corresponding to the collocated sensors-actuators. Moreover the dynamics of a high number of modes is needed to verify possible spillover. If the controller pass band frequency is 500 Hz, then the modal frequencies should encompass modes up to the double at least, to be sure of no spillover. The three free translation of the satellite were removed by deleting the relative rigid modes, while the three rotational rigid modes have been kept

to allow the inclusion of the satellite attitude control system. In space the only damping is the structural one, so to be conservative a 0.005 modal damping factor has been assigned to each mode. This brings to a quite different situation with respect to ground telescopes, where damping can be significantly greater thanks to the presence of air between the mirror and the back-plate. This implies that only the controller can supply the damping guaranteeing stability. The two first order dynamic systems used to describe the actuators and sensors dynamics were both set at 500 Hz, so practically setting the mirrors control bandwidth. On one hand the internal dynamic of these systems can be faster, thus allowing to introduce less delay, on the other a lower control frequency bandwidth could reduce the spillover effects on the higher frequency modes. So these filters can acquire a double meaning, the introduction of actuators and sensors delay, and the presence of anti-spillover filters that attenuate the controller excitation of higher frequencies. In this sense the frequencies of these filters are important project parameters that represent a compromise between the controller delays and spillover attenuation.

4 High frequencies recovery through residualization

During the simulation a static recovery of the high frequencies, not modeled in the dynamics of the satellite, can be performed so that when the controller reaches a steady position at the end of the commanded shapes they are not affected by the number of modes used. It should be noted that the high frequencies recovery is implemented only for mirrors scalar points and not for the satellite free rotation, because the related improvement is negligible for the attitude control system. In the following equations we will remove the three free rotational motions because they do not affect the modal stiffness. So we can think that the satellite is fixed in space without any mistake. The simulation of the mirrors control system works with assigned final commanded position, so the difference between a modal truncation and the related static residualization will appear in the forces needed to reach the final steady state. The static residualization can be seen from two different points of view, both leading to the same result. The first interpretation divides low and high frequency modes, recovering the latter with a static approach:

$$\{S\} = [X_l | X_h] \left\{ \begin{array}{c} q_l \\ q_h \end{array} \right\} = X_l q_l + X_h q_h \tag{18}$$

Writing the system static equilibrium equations, and assuming $F = F^C + F^A + F^e$, we find:

$$\left[\omega^2\right] q = X^T F \tag{19}$$

$$q = \left[\omega^2\right]^{-1} X^T F \tag{20}$$

$$S = X \left[\omega^2\right]^{-1} X^T F \tag{21}$$

The physical flexibility matrix condensed at the scalar points S can be thus obtained from the modal matrices as:

$$\overline{K}^{-1} = X \left[\omega^2\right]^{-1} X^T = X_l \left[\omega_l^2\right]^{-1} X_l^T + X_h \left[\omega_h^2\right]^{-1} X_h^T \tag{22}$$

This implies that we can write the high frequency stiffness modal contribution as a function of low frequency modes and the condensed stiffness in physical degrees of freedom:

$$X_h \left[\omega_h^2\right]^{-1} X_h^T = \overline{K}^{-1} - X_l \left[\omega_l^2\right]^{-1} X_l^T \tag{23}$$

Now if we write the modal equations system by assuming that the high frequencies contributions act statically at low frequencies:

$$\begin{cases} \ddot{q}_l + [C_l]\dot{q}_l + \left[\omega_l^2\right] q_l = X_l^T F \\ \left[\omega_h^2\right] q_h = X_h^T F \end{cases} \tag{24}$$

so that by using the second set of equations to substitute q_h in equation 18, we obtain:

$$S = X_l q_l + X_h \left[\omega_h^2\right]^1 X_h^T F \tag{25}$$

Putting equation 23 into equation 25 we find the final expression for the relative displacements S with high frequencies residualization:

$$S = X_l q_l + \left(\overline{K}^{-1} - X_l \left[\omega_l^2\right]^{-1} X_l^T\right) F \tag{26}$$

The same result can be reached with a different approach based on acceleration modes, i.e. the one that is more commonly used by structural engineers. Before the condensation at the scalar points the system equation can be written as:

$$M\ddot{S}_g + C\dot{S}_g + KS_g = F_g \tag{27}$$

$$S_g = K^{-1}\left(F_g - M\ddot{S}_g - C\dot{S}_g\right) \tag{28}$$

Then it is possible to substitute the acceleration and speed values with those calculated through the low frequency modal reduction:

$$\begin{aligned} S_g &= -K^{-1}MX_{g_l}\left(X_{g_l}^T F_g - \left[\omega_l^2\right] q - [2\varepsilon_l\omega_l]\,\dot{q}_l\right) - K^{-1}CX_{g_l}\dot{q}_l + K^{-1}F_g = \\ &= K^{-1}MX_{g_l}\left([2\varepsilon_l\omega_l]\dot{q}_l + [\omega_l^2]q_l\right) - K^{-1}CX_{g_l}\dot{q}_l + \left(K^{-1} - K^{-1}MX_{g_l}X_{g_l}^T\right)F_g \end{aligned} \tag{29}$$

The modal eigenvalues problem can be written in canonical form as:

$$K^{-1}MX_g = X_g\left[\frac{1}{\omega^2}\right] \tag{30}$$

so

$$K^{-1}MX_{g_l} = X_{g_l}\left[\omega_l^2\right]^{-1} \tag{31}$$

Putting equation 31 into equation 29 we find:

$$S_g = X_{g_l}q_l + \left(K^{-1} - X_{g_l}[\omega_l^2]^{-1}X_{g_l}^T\right)F_g + X_{g_l}[\omega_l^2]^{-1}[2\varepsilon_l\omega]\dot{q}_l - K^{-1}CX_{g_l}\dot{q}_l \tag{32}$$

By assuming a diagonal modal damping and remembering equation 22, we can demonstrate that the two final damping terms become void:

$$\begin{aligned} &X_{g_l}[\omega_l^2]^{-1}[2\varepsilon_l\omega_l]\dot{q}_l - K^{-1}CX_{g_l}\dot{q}_l = \\ &= X_{g_l}[\omega_l^2]^{-1}X_{g_l}^T CX_{g_l}\dot{q}_l - X_{g_l}[\omega_l^2]^{-1}X_{g_l}^T CX_{g_l}\dot{q}_l - X_{g_h}[\omega_h^2]^{-1}X_{g_h}^T CX_{g_l}\dot{q}_l = \\ &= -X_{g_h}[\omega_h^2]^{-1}X_{g_h}^T CX_{g_l}\dot{q}_l = 0 \end{aligned} \tag{33}$$

The last term of the previous equation is zero because we have a diagonal modal damping that implies orthogonal eigenvectors through the physical damping matrix. Moreover if we consider that in our model the external forces are applied only through actuators, and so through scalar points, it is possible to equal the virtual work done by the global forces F_g and by the condensed scalar points forces F:

$$\delta S_g^T F_g = \delta S^T F \tag{34}$$

$$\delta S_g^T F_g = \delta S_g^T U^T F \tag{35}$$

so we can state that:

$$F_g = U^T F \tag{36}$$

Applying to equation 32 the extraction matrix U and considering relation 36 we have:

$$\begin{aligned} US_g &= UX_{gl}q_l + \left(UK^{-1}U^T - UX_{gl}[\omega_l^2]^{-1}X_{gl}^T U^T\right) F & (37)\\ S &= Xq_l + \left(UK^{-1}U^T - X_l[\omega_l^2]^{-1}X_l^T\right) F & (38) \end{aligned}$$

Using the definition of U, $S = US_g$, equation 36, and the static equilibrium equation $S_g = K^{-1}F_g$, we obtain

$$S = US_g = UK^{-1}F_g = UK^{-1}U^T F, \tag{39}$$

showing that $UK^{-1}U^T$ is equal to the inverse of the stiffness matrix $\overline{K}^{-1}$ condensed at the scalar points. Equation 38 can now be rewritten as:

$$S = Xq_l + \left(\overline{K}^{-1} - X_l[\omega_l^2]^{-1}X_l^T\right) F \tag{40}$$

that is the same result obtained in equation 26. The simulation program requires $\overline{K}^{-1}$ as an input, this matrix can be obtained by a FEM analysis solving n_a times the condensed static problem with n_a unit load applied at the scalar points degrees of freedom. A possible source of trouble could be the need to put the physical flexibility in mean axes, to be coherent with the modal terms. We can safely avoid such an operation because the scalar points are defined as relative movements between grid points, so the choice of a particular coordinate system has no effect on the related flexibility matrix calculation.

5 Static condensation approach

The structure modal description shown in the previous two sections is not the only possible way to obtain a reduced set of equations describing the satellite behavior. Another solution could come from the static condensation of the Finite Element Model on appropriate physical degrees of freedom. For example the degrees of freedom of the nodes representing the displacements useful to simulate the satellite control systems, i.e. at the point and in the direction of application of the actuators forces.

The FEM precise dynamic equations of the satellite structure can be written as:

$$M\ddot{S}_g + C\dot{S}_g + KS_g = F_g^C + F_g^A + F_g^e \tag{41}$$

It is possible to choose and then to separate the dynamic degrees of freedom from the static ones:

$$\begin{bmatrix} M_{dd} & M_{ds} \\ M_{sd} & M_{ss} \end{bmatrix} \begin{Bmatrix} \ddot{S}_d \\ \ddot{S}_s \end{Bmatrix} + \begin{bmatrix} C_{dd} & C_{ds} \\ C_{sd} & C_{ss} \end{bmatrix} \begin{Bmatrix} \dot{S}_d \\ \dot{S}_s \end{Bmatrix} + \begin{bmatrix} K_{dd} & K_{ds} \\ K_{sd} & K_{ss} \end{bmatrix} \begin{Bmatrix} S_d \\ S_s \end{Bmatrix} = \begin{Bmatrix} F^C + F^A + F_d^e \\ F_s^e \end{Bmatrix} \tag{42}$$

Now an Irons-Guyan reduction can be applied to the previous equations to obtain a system reduced at the dynamic degrees of freedom only:

$$\tilde{M}\ddot{S}_d + \tilde{C}\dot{S}_d + \tilde{K}S_d = F^C + F^A + \tilde{F}^e \tag{43}$$

where

$$\begin{aligned} \tilde{K} &= K_{dd} - K_{ds}K_{ss}^{-1}K_{sd} & (44)\\ \tilde{M} &= M_{dd} - M_{ds}K_{ss}^{-1}K_{sd} - K_{ds}K_{ss}^{-1}\left(M_{sd} - M_{ss}K_{ss}^{-1}K_{sd}^{-1}\right) & (45) \end{aligned}$$

while the damping matrix $\tilde{C}$ can be thought as proportional to the stiffness: $C \div K$. The state system can be written as:

$$\left\{ \begin{array}{c} \ddot{S}_d \\ \dot{S}_d \end{array} \right\} = \left[\begin{array}{cc} -\tilde{M}^{-1}\tilde{C} & -\tilde{M}^{-1} \\ I & 0 \end{array} \right] \left\{ \begin{array}{c} \dot{S}_d \\ S_d \end{array} \right\} + \left[\begin{array}{c} \tilde{M}^{-1} \\ 0 \end{array} \right] \tilde{F} \tag{46}$$

These state matrices are different with respect to the modal ones because they are not diagonal but fully coupled and require the inversion of the reduced mass matrix. The output can be expressed as:

$$S = US_g = US_d + US_s = US_d \tag{47}$$

because all the degrees of freedom of interest for the control systems simulation can be considered as dynamic ones.

The advantages linked with the static model reduction are:

- The possibility to write a simpler simulation program.
- The displacements of the degrees of freedom are not obtained in mean axis but in a fixed reference system. This could simplify the interpretation of the results, especially when absolute nodes displacements are requested.
- The simulation is always correct from the static point of view without using any residualization process.
- The number of dynamic degrees of freedom could be lower then the numbers of normal modes required to have a good system representation.

The negative aspects can be resumed as:

- The impossibility to perform the state system integration with the transition matrices because the state matrix is fully coupled. This means higher computational time.
- The need to verify that the static reduction does not change the dynamic properties of the system. In particular it should be verified that the normal modes of the global model are the same as the static reduced ones, at least in the frequency range of interest. If this is not the case some other dynamic degrees of freedom have to be introduced to obtain a better model reduction from the dynamic point of view.
- There is not a simple way to determine the reduced matrix for the structural damping.

On the base of these considerations we have decided to use the normal modes approximation, to assure a better simulation efficiency and an easier determination of the structural damping. Moreover by using all the normal modes inside the frequency range of interest we have the certainty to obtain a very good dynamic model.

6 Satellite attitude control low

In this work the satellite attitude control system does not represent an important goal to achieve, but we are interested to verify the absence of possible negative interactions between it and the mirrors controllers. So we have decided to choose a simple control law based on a PD action, making also some approximations to simplify the problem. For example we have not introduced attitude actuators and sensors dynamics and we have considered an ideally collocated situation,

Control Frequency (ω_A)	4 Hz
K_P^A	50
K_D^A	700

Table 1: Attitude control parameters resume.

where the attitude control couples are applied directly to the mean principal inertia axes with the attitude angles being rotations around the very same mean axes. The only constraint that has been set is the maximum allowable control couple that can be used i.e.: 0.1 Nm. As it is possible to appreciate looking at equations 13 and 16, the interaction between the two control systems is not related to the modal state matrix, which is fully uncoupled, but comes through the modal forces and the modal recovery of the physical displacements. This means that the attitude control system can be seen as a possible source of external disturbances for the active mirror controller.

The attitude feedback control couples can be expressed as:

$$f_i^A = K_P^A(p_i^{req} - p_i^{mes}) + K_D^A \dot{p}_i^{mes} \tag{48}$$

where $i = 1 \dots n_{rr}$ and p_i refers to the three rigid rotation of the center of mass. The controller frequency has been set to 4 Hz, a value higher than needed, in order to worsen possible interactions with the deformable mirror controls. Random noises are added to the control moments and measured angles. Moreover the actuators saturation is taken into account assuring to not overcame the limit couples of 0.1 Nm. Table 1 resumes the main parameters of the attitude control system.

7 Active mirrors control law

The mirror control forces can be split in two parts, one related to a PD2 feedback control law and another related to a feedforward open loop contribution.

The general PD2 control forces are written as:

$$F_{1_i}^C = K_{P_i}\,(p_i^{req} - p_i^{mes})^\alpha + K_{Da_i}(\dot{p}_i^{mes})^\beta + K_{D2a_i}\ddot{p}_i^{mes} + K_{Db_i}(\dot{p}_i^{req})^\beta + K_{D2b_i}\ddot{p}_i^{req} \tag{49}$$

where the index $i = 1 \dots n_a$ refers to the actuators number. The parameters K_{Db} and K_{D2b} allow to improve the control flexibility, i.e.:

- $K_{Db} = 0$, $K_{D2b} = 0$ control in velocity and acceleration;
- $K_{Da} = -K_{Db}$, $K_{D2a} = -K_{D2b}$ control in velocity and acceleration error;
- control with arbitrary setting of previous gains could be seen as a trial to introduce feedforward terms on requested positions, velocities and accelerations. We will return to the gains related to $\dot{p}^{req}$ and $\ddot{p}^{req}$ later on, i.e. when we describe static and dynamic feedforward terms.

The exponents α and β allow to introduce a nonlinear control behavior on proportional and derivative terms. The simulation program allows to introduce the same gains for all the actuators, or scaling their proportional and derivative terms from the diagonal stiffness values. So K_{P_i} andK_{Da_i} can assume a constant value or can be expressed as:

$$K_{P_i} = K_P \left(\frac{\overline{K}_I^{ii}}{max(\overline{K}_{diag})} \right)^\gamma \tag{50}$$

$$K_{Da_i} = K_{Da} \left(\frac{\overline{K}_I^{ii}}{max(\overline{K}_{diag})} \right)^\gamma \tag{51}$$

where $\overline{K}_I$ is the system identified stiffness matrix condensed at the control points, namely the same matrix needed to calculate the static feedforward term, (equation 56). K_P and K_{Da} are two user input parameters, and γ is an exponent allowing to better scale the gains. When there are important differences in diagonal stiffness values a simple linear weighting can brings to an unstable behavior and γ can become an important nonlinear scaling factor to avoid this problem.

Anyway the control here used will be linear ($\alpha = 1$, $\beta = 1$) and the proportional and derivative gains are constant on each actuator ($\gamma = 0$). The PD2 term can thus be written as:

$$F_{1_i}^C = K_P(p_i^{req} - p_i^{mes}) + K_{Da}\dot{p}_i^{mes} + K_{D2a}\ddot{p}_i^{mes} \tag{52}$$

The first and second derivative with respect to time in equation 52 are obtained using two first order filters:

$$\dot{p}^{mes} = \frac{\omega_V}{s+\omega_V} s p^{mes} \tag{53}$$

$$\ddot{p}^{mes} = \frac{\omega_V}{s+\omega_V} s \dot{p}^{mes} \tag{54}$$

$$\tag{55}$$

where ω_V must be chosen by compromising between bandwidth and noise attenuation (see table 2).

The PD2 term alone is not adequate in providing the required control precision with a sufficient bandwidth because its gains are limited by stability. The presence of an integral term would not improve control performance without endangering stability, so the requested precision can be achieved only by an appropriate feedforward. The simplest feedforward scheme can be seen as the force needed to obtain a commanded steady state balanced position for the mirror, i.e. the static response. So the static feedforward contribution allow to reach the commanded mirror position and the PD2 feedback action gives the necessary dynamic performance and the fundamental system damping to satisfy bandwidth requirements. Assuming to know the true structural stiffness matrix $\overline{K}$ condensed at the control points, the feedforward forces related to a requested mirror shape p^{req} can be expressed as:

$$F_2^C = \overline{K} p^{req} \tag{56}$$

or in incremental form

$$F_{2_{k+1}}^C = \bar{f}_k + \overline{K}(p^{req} - \bar{p}_k) \tag{57}$$

where $\bar{f}_k$ is the steady force reached at the command time t_k, and $\bar{p}_k$ is the static response position. This assumption is correct if the controller assures to reach the requested position at the end of every command step. However $\overline{K}$ is not known, and even the true static position is not precisely measurable because of the presence of environmental disturbances and sensors and actuators noises. For this it is necessary to introduce an identification process (described in section 9) to simulate the experimental determination of the stiffness matrix trough the use of a least square approximation. Such a simulation requires removing the possible presence of rigid motions between the mirrors and their back-plates and this is the reason of the low control action stiffness put in the finite element model, cited in the opening section. This stiffness must be negligible compared to the proportional control gains, because its presence should only remove stiffness singularities without changing the model properties. It must be noted though that rigid body motions do not affect the actual experimental identification since the related procedure can deal with free mirrors. It is also necessary to be able to measure the static response position $\bar{p}$ and force $\bar{f}_k$. They can be obtained trough a simple average of the positions and forces related to the final, stabilized, part

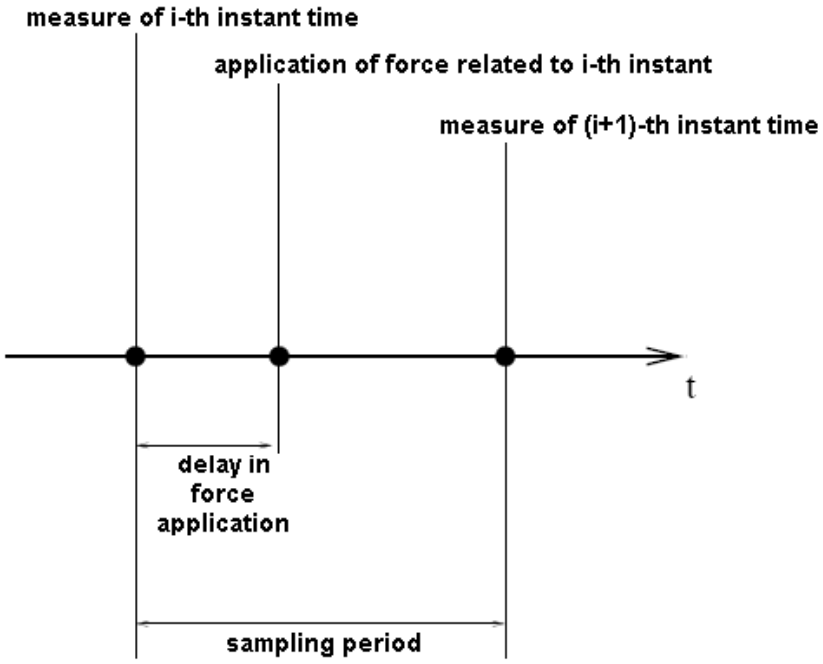

(a) Application of control force with delay respect to measure time.

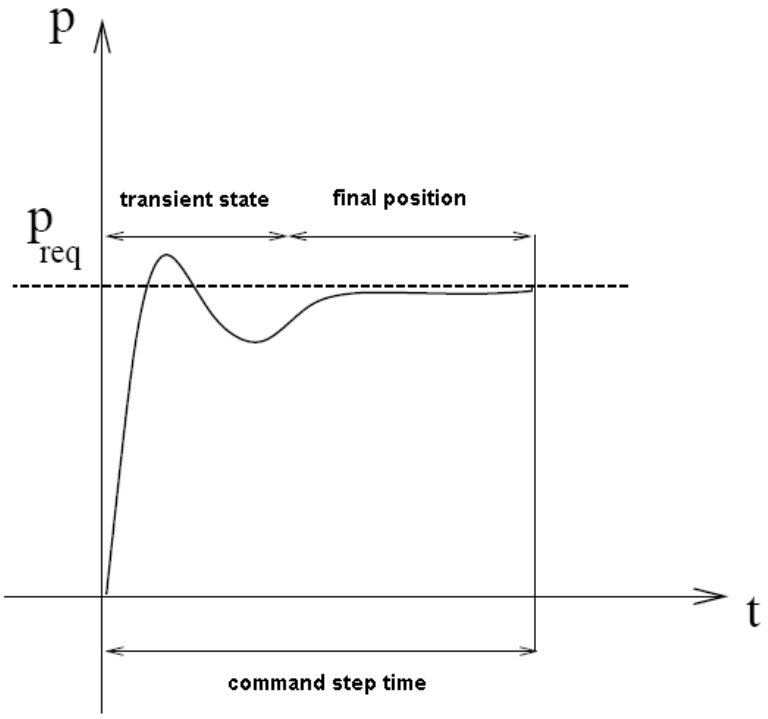

(b) Sketch of a typical control behavior on commanded step.

Figure 4: Control action.

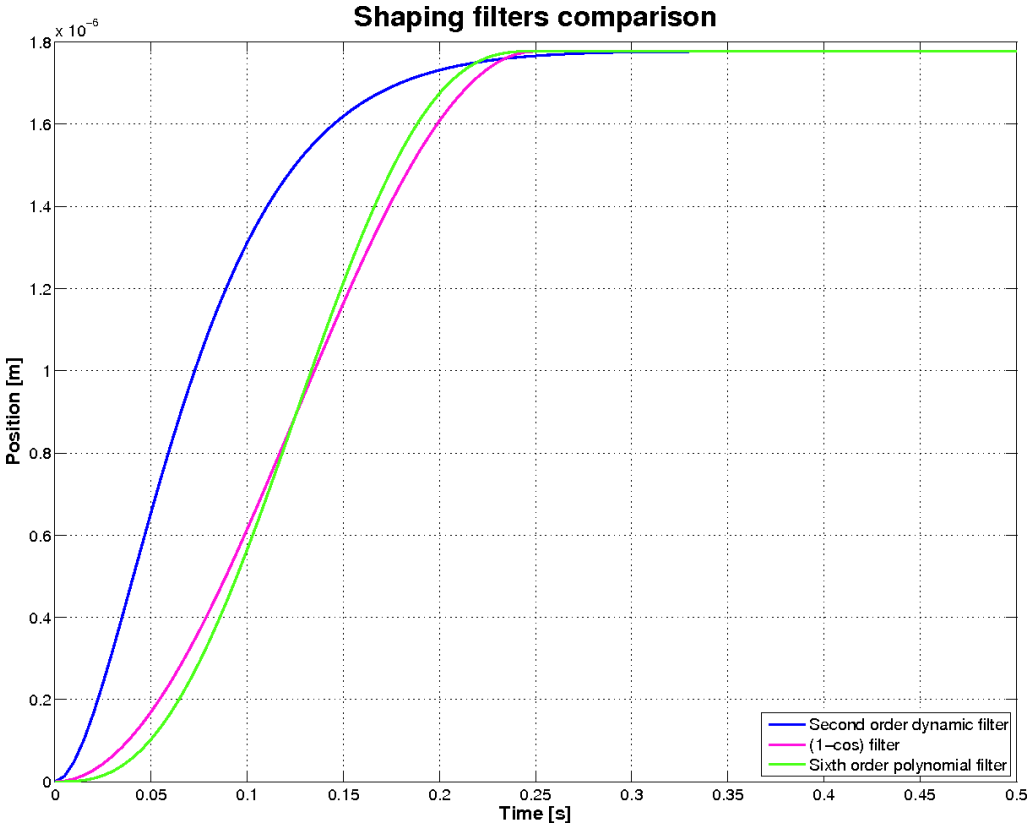

Figure 5: Shaping filters comparison.

of the command step, i.e. when the static final position has been reached. To avoid sudden high changes of the control forces two shaping filters are applied to the command steps and to the feedforward forces. The program allows to use either a second order shaping filter or two different kinds of algebraic profiles (see figure 5): a sixth order polynomial filter, and a $(1 - cos)$ filter. The two filters frequencies can be chosen independently, accordingly to the control needs. This implies that the requested position p^{req} has an imposed transient state, so it is possible to exploit the feedforward concept with some time blended profiling to improve dynamic control performances during transients:

$$F_{3_i}^C = K_{Db_i}(\dot{p}_i^{req})^\beta + K_{D2b_i}\ddot{p}_i^{req} \tag{58}$$

where K_{Db} and K_{D2b} can be interpreted as a lumped feedforward aimed at the cancellation of system inertia and damping. It has been speculated that by using fully coupled mass and damping matrices we could have achieved a more ideal cancellation of the system dynamics. For a sound implementation such an approach should not rely on the related theoretical terms but use experimentally identified mass and damping matrices, an uncertain and difficult undertaking indeed. Moreover it would lead to a controller coupling all of the degrees of freedom dynamically. This coupling in turn would mean a higher, likely unbearable, computational effort and a higher identification time before starting telescope observations. So we have chosen to simplify the approach by considering a lumped dynamic feedforward, i.e. assume diagonal mass and damping matrices. If the actuators are roughly uniformly distributed the lumped mass matrix term related to the i^{th} degree of freedom can be estimated by simply dividing the mirror mass by the actuators number. In this manner we obtain a constant term for each mirror, so avoiding the need to identify the mass matrix. The lumped feedforward for the damping is somewhat more difficult to estimate but,

assuming a diagonal modal damping we can approximate the physical one as proportional one, i.e. a linear combination of mass and stiffness matrices. Presently the simulation program supports different dynamic feedforward gains expressions:

- two constant coefficients for all the actuators, neglecting the coupling and any physical interpretation
$$F_{3_i}^C = K_{Db}(\dot{p}_i^{req})^\beta + K_{D2b}\ddot{p}_i^{req} \tag{59}$$
- a diagonal mass $\overline{M}$ matrix and a diagonal identified stiffness matrix $\overline{K}_{I_{diag}}$ to scale the gains
$$F_{3_i}^C = \left(K_{Db}^m \overline{M}^{ii} + K_{Db}^k \overline{K}_{I_{diag}}^{ii}\right)(\dot{p}_i^{req})^\beta + K_{D2b}\overline{M}^{ii}\ddot{p}_i^{req} \tag{60}$$
- a diagonal mass $\overline{M}$ and a complete stiffness matrix $\overline{K}_I$
$$F_{3_i}^C = K_{Db}^m \overline{M}^{ii}(\dot{p}_i^{req})^\beta + K_{Db}^k \overline{K}_I(\dot{p}^{req})^\beta + K_{D2b}\overline{M}^{ii}\ddot{p}_i^{req} \tag{61}$$

The requested velocity $\dot{p}^{req}$ and acceleration $\ddot{p}^{req}$ can be calculated analytically on the base of the shaping profiles previously mentioned. In this project we have chosen to use the first feedforward scheme listed above, with different gain values to differentiate the central mirror from petals. Anyway, as we will show later on, the gain K_{Db} on petals and on central mirror corresponds quite well to the relative lumped mass matrix term. Obviously β has been set to unit for the feedforward term too.

So the final incremental control force implemented in our specific case can be written as:

$$F_{k+1}^C = \bar{F}_k + F_{1_k}^C + F_{2_k}^C + F_{3_k}^C =$$
$$= \bar{F}_k + K_P(p^{req} - p_k) + K_{Da}\dot{p}_k^{mes} + K_{D2a}\ddot{p}_k^{mes} + \overline{K}_I(p^{req} - \bar{p_k}) + K_{Db}(\dot{p}_k^{req}) + K_{D2b}\ddot{p}_k^{req} \tag{62}$$

It's important to note that the different control terms act at different frequencies. In fact the PD2 control action works at control frequency, while the feedforward follows the lower command step frequency. This is a key factor for the control system, because it allows to apply a fully uncoupled high frequency control trough the PD2, and to introduce the control coupling using the structural stiffness trough the feedforward contribution at a lower frequency.

The computation and A/D/A conversions introduce errors and delays on the control forces that are appropriately modeled in the simulation program. In fact the control forces applied during acquisition, computation and conversion time are the same as those of the previous step and not the new ones. Such a delay in the application of forces can be set as a fraction of the sampling period. Moreover sensors, actuators and A/D/A conversions introduce errors that are modeled as wide band noises and quantization errors. The program simulate them by adding Gaussian noises and quantization errors to measures and control forces, appropriately scaled in relation to quantization resolution and input/output ranges. All of these parameters can be set by the user. To limit the effect of time delays in the application of control forces the controller implements a further compensation in the form of a parabolic extrapolation:

$$F_{k+1}^{Capp} = \delta F_k^{Capp} + (\epsilon F_{k+1}^C + \zeta F_k^C + \eta F_{k-1}^C) \tag{63}$$

where F_k^{Capp} is the real control force applied to the mirror at time t_k, $F_{k+1}^C, F_k^C, F_{k-1}^C$ are the computed control forces at times t_{k+1}, t_k, t_{k-1} respectively and $\delta, \epsilon, \zeta, \eta$ are parameters calculated on the base of the time delay.

The control system frequency has been set to 4000 Hz, to have a sufficiently large control bandwidth for the simulated filters and compensators, while the command step has been set to

2 Hz. The initial suggestions of a 500 Hz control frequency and 1 Hz command steps was proven soon to be inadequate to satisfy specifications, mainly because it was not able to encompass a wide enough dynamic contents of the system to ensure adequate stability with the relatively many vibration modes involved. The above figures have been determined after some tests with lower control frequencies aimed at granting the required accuracy of 200 nm. It has been seen that 2800 Hz represents the lower control frequency limit with a 2Hz command step, while 1600 Hz is the limit with 1 Hz command step. The chosen frequency of 4000 Hz allows to maintain a higher response quality and a safe margin to account for the approximations introduced in the model. Note that higher control frequencies should be even better but were ruled out because of power constraints. It must be noted that even if the command step frequency is not high, we have to control and quickly damp transient commands. So a sufficiently large control bandwidth is required to avoid instabilities independently from the command step length. The derivative filter has a cut off frequency of 500 Hz as a good compromise to avoid high delays and noise amplification. The feedforward forces and commanded positions are pre-shaped with geometric filters, both at 4 Hz frequencies, i.e. half of command step time. The standard deviations of Gaussian noises are 1.0E-5 N for the forces and 30.0E-9 m for the positions. The quantization errors are calculated for 16 bits, assuming ± 0.0005 m as the range of positions to be measured and ± 0.2 N as the range of actuators forces. The quantization errors represent an important factor in determining controller performances and stiffness identification quality. There are two main causes linked to this:

- the position sensors need a large range because after the initial petals deployment phase the control has to act on mirrors rigid motions assuring the correct position of each petals with respect to the central mirror. Clearly this request implies larger motions capabilities than the operational demand for mirror deformation. So the position resolution is 15 nm and represents a first limit on the precision available for the controller.

- the low system damping, together with the need of a low control frequency to save power, does not allow to have high PD2 gains, so the feedback forces could be some orders of magnitude lower than the feedforward ones. This implies that the force quantization error can significantly modify the PD2 ideal forces values and, in turn, this means lower dynamic performances of the control. The final result is a sort of bang-bang controller.

- the high noise level and quantization error affect steady force and position measurements during the stiffness matrix identification process. This leads to a poor quality of the identified stiffness matrix and, as a consequence, to large errors in achieving the commanded steady positions.

It's important to underline that even if quantization and noise are not negligible factors, they are not so important in determining the control frequency, that is primarily affected by low system damping and high frequency dynamic excitation during control action.

To determine the controller PD2 gains two step were followed. First standard Ziegler-Nichols tuning rules have been used to obtain a starting value of the PD terms. Then an optimization of these gains has been performed via a MonteCarlo method. The final gains and controller properties obtained with different control and command frequencies are summarized in table 2.

Control Frequency (ω_c)	4000 Hz	2800 Hz	1600 Hz
Command frequency (ω_{cmd})	2 Hz	2 Hz	1 Hz
Actuators filter frequency	500 Hz	500 Hz	300 Hz
Sensors filter frequency	500 Hz	500 Hz	300 Hz
Derivation filter frequency (ω_V)	500 Hz	500 Hz	300 Hz
Force application delay	$\frac{2}{\omega_c}$ s	$\frac{2}{\omega_c}$ s	$\frac{2}{\omega_c}$ s
K_P	1000	700	350
K_{Da}	12	10	5
K_{D2a}	0.0008	0	0
K_{Db}(petals)	5	5	5
K_{D2b}(petals)	0.12	0.12	0.12
K_{Db}(central)	12	12	12
K_{D2b}(central)	0.2	0.2	0.2

Table 2: Control parameters resume.

8 Solution convergence and Sub-stepping technique

The feedforward contribution allows to reach the exact steady position only if the identified stiffness matrix is the ideal one but, as we will see in section 9, the identification process can only give an approximation of the system stiffness. So to improve the controller precision in reaching the requested final position we can think to update the static feedforward term more times inside a single command step, as shown in figure 6. Obviously this solution, that we will call sub-stepping technique, requires sufficiently good dynamic performances, because the controller must be able to quickly reach the steady position to allow computing the force and position average needed to calculate the following feedforward action. Anyway we have no guarantee about the use of an estimated stiffness matrix in determining the feedforward contribution. So we would like to know the effect of possible inaccuracies related to the stiffness identification.

Supposing to use sub-stepping technique, once the system has reached a steady state position $\bar{p}_{k+1}$ thanks to PD2 action, the control system force can be written in an incremental form:

$$F^C_{k+1} = [K_P](p_{req} - \bar{p}_{k+1}) + \bar{F}_k + \overline{K}_I(p_{req} - \bar{p}_k) \tag{64}$$

where the index k refers to the sub-steps inside the main command step. The applied force can always be rewritten as a product between real stiffness and reached position:

$$\overline{K}\bar{p}_{k+1} = [K_P](p_{req} - \bar{p}_{k+1}) + \bar{F}_k + \overline{K}_I(p_{req} - \bar{p}_k) \tag{65}$$

from which

$$(\overline{K} + [K_P])\bar{p}_{k+1} = \bar{F}_k - \overline{K}_I\bar{p}_k + ([K_P] + [\overline{K}_I)p_{req} \tag{66}$$

The average force $\bar{F}$ can be expressed in function of real stiffness and average position too:

$$(\overline{K} + [K_P])\bar{p}_{k+1} = (\overline{K} - \overline{K}_I)\bar{p}_k + ([K_P] + [\overline{K}_I)p_{req} \tag{67}$$

Equation 67 can be written in a more compact form as:

$$\bar{p}_{k+1} = [A]^{-1}[\Delta K]\bar{p}_k + [A]^{-1}[B]p_{req} \tag{68}$$

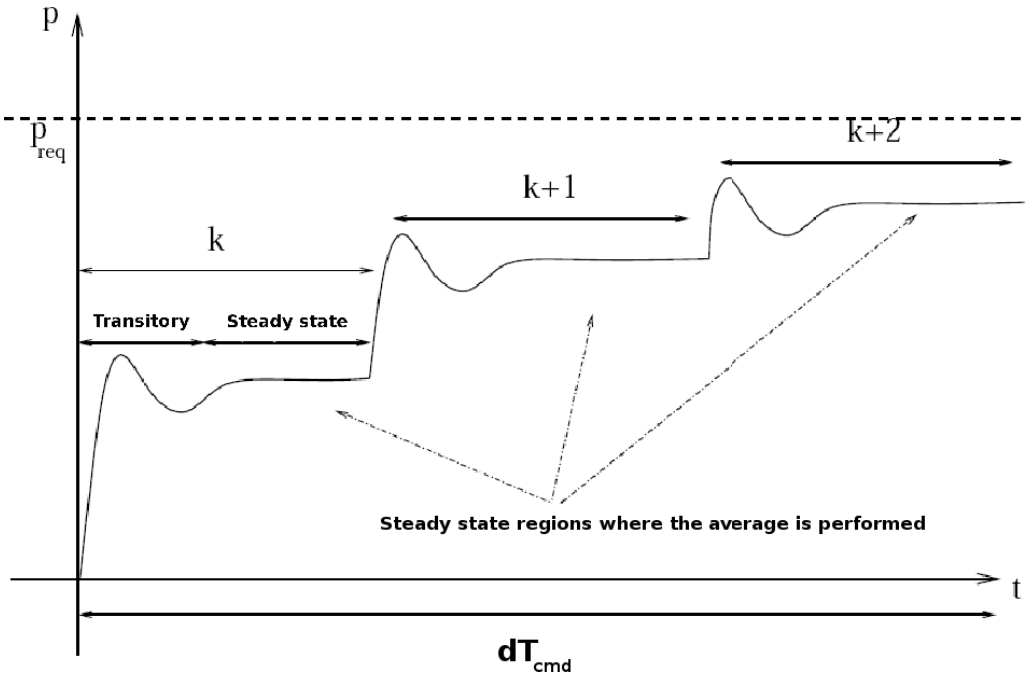

Figure 6: Feedforward term can be updated more times inside the single command step through the sub-stepping technique.

where

$$[A] = (\overline{K} + [K_P]) \tag{69}$$

$$[\Delta K] = (\overline{K} - \overline{K}_I) \tag{70}$$

$$[B] = ([K_P] + \overline{K}_I) \tag{71}$$

The solution of the difference equation 68 can be obtained as the sum of an homogeneous and a particular solution:

$$\bar{p}_k = u_k + v_k \tag{72}$$

The homogeneous equation is:

$$u_{k+1} = [A]^{-1}[\Delta K]u_k \tag{73}$$

and the relative solution matches:

$$u_k = G[\rho^k]G^{-1}u_0 \tag{74}$$

where the diagonal matrix $[\rho]$ and the transformation matrix G are simply the eigenvalues and eigenvectors obtained from the matrix $([A]^{-1}[\delta K])$, while u_0 is linked with the given initial conditions as we will see later. The particular solution can be simply achieved considering that the forcing term $[A]^{-1}[B]p_{req}$ is constant. So we can try to find a particular solution that is constant too:

$$v = [A]^{-1}[\Delta K]v + [A]^{-1}[B]p_{req} \tag{75}$$

i.e.

$$v = (I - [A]^{-1}[\Delta K])^{-1}[A]^{-1}[B]p_{req} = [C]p_{req} \tag{76}$$

Through relations 69, 70 and 71, $[C]$ can be written as:

$$[C] = \left(I - (\overline{K} + [K_P])^{-1}(\overline{K} - \overline{K}_I)\right)^{-1}\left((\overline{K} + [K_P])^{-1}([K_P] + \overline{K}_I)\right) \tag{77}$$

Moreover we can say that:

$$\left([K_P] + \overline{K}_I\right) = \left([K_P] + \overline{K}_I + \overline{K} - \overline{K}\right) = \left(\overline{K} + [K_P]\right) - \left(\overline{K} - \overline{K}_I\right) \tag{78}$$

If we put equation 78 in 77 we obtain:

$$\begin{aligned} [C] &= \left(I - (\overline{K} + [K_P])^{-1}(\overline{K} - \overline{K}_I)\right)^{-1} \left((\overline{K} + [K_P])^{-1} \left((\overline{K} + [K_P]) - (\overline{K} - \overline{K}_I)\right)\right) = \\ &= \left(I - (\overline{K} + [K_P])^{-1}(\overline{K} - \overline{K}_I)\right)^{-1} \left(I - (\overline{K} + [K_P])^{-1}(\overline{K} - \overline{K}_I)\right) = I \end{aligned} \tag{79}$$

So the general solution 72 can be expressed as:

$$\bar{p}_k = G[\rho^k]G^{-1}u_0 + p_{req} \tag{80}$$

Moreover if we choose $u_0 = (p_0 - p_{req})$ we find the solution that satisfy the initial condition p_0:

$$\bar{p}_k = G[\rho^k]G^{-1}(p_0 - p_{req}) + p_{req} \tag{81}$$

It is evident from equation 81 that if each element of diagonal matrix $[\rho]$ is below the unit value the solution converges to the requested position p_{req}:

$$\rho_i < 1 \qquad \Longrightarrow \qquad \lim_{k\to\infty} \bar{p}_k = p_{req} \tag{82}$$

This means that the solution convergence is linked with the spectral radius of matrix $([A]^{-1}[\Delta K])$, faster convergence implies spectral radius lower than unit. We can say that:

$$\begin{aligned} max\|\rho\| = sr([A]^{-1}[\Delta K]) &= sr\left((\overline{K} + [K_P])^{-1}(\overline{K} - \overline{K}_I)\right) = \\ &= sr\left((I + \overline{K}^{-1}[K_P])^{-1}\overline{K}^{-1}(\overline{K} - \overline{K}_I)\right) \leq \\ &\leq sr\left((I + \overline{K}^{-1}[K_P])^{-1}\right) sr\left((I - \overline{KK}_I)\right) \leq 1 \end{aligned} \tag{83}$$

where $sr(A)$ is the spectral radius of the matrix A. The spectral radius of $(I + \overline{K}^{-1}[K_P])$ is always greater than one because it is the sum of two positive terms and one of them is the identity matrix, so the inverse of this matrix, that is the first term of 83, has clearly a spectral radius less than one. The second term of equation $(I - \overline{KK}_I)$ has a sr less than unit even if the matrix $\overline{K}_I$ has been roughly estimated. If we could have $\overline{K}_I \equiv \overline{K}$ we would obtain an instantaneous convergence. To note that even without the $\overline{K}_I$ matrix the convergence is guaranteed

$$[A]^{-1}[\Delta K] = (I + \overline{K}^{-1}[K_P])^{-1}(I) \tag{84}$$

because the term expressed in equation 84 has a sr less than unit. But the convergence speed in this case would be lower, so its necessary to use identified stiffness matrix.

We have just demonstrated that the application of feedforward term more times inside the command step assures the solution convergence even with a roughly estimated stiffness matrix. The sub-stepping technique can be seen as the division of the command length in sub-steps where the requested position remains constant, so it is a sort of high frequency application of slower-acting commands. But as we have underlined at the beginning of this section, the sub-stepping requires good dynamic control performance to be applied. The LIDAR satellite system has low passive damping, only the structural one, and so low PD2 gains. As we have seen in section 7 the controller can't provide high dynamic performances without higher control frequencies. This makes it difficult to apply with success the sub-stepping technique in our project. For this reason we have only one iteration to reach a sufficiently precise final steady position and, obviously, this constraint leads to the requirement of a sufficiently good identified stiffness matrix.

9 Identification

As underlined in the previous section there is almost no possibility to exploit the sub-stepping procedure, so a good identification of the stiffness matrix is required to obtain acceptable shaping performances. Such an identification can be carried out by retrieving from the local control units a set of averaged position and the related force commands to set up a least squares system of equations that is recursively solved to update the identified stiffness matrix in real time, thus allowing an adaptation to relatively slow system and disturbances modifications. The duration of the shape commands must be long enough to insure that there remains a sufficient time length to allow the averaging of the steady positions and forces. The command time has to guarantee an adequate signal-to-noise ratio for the estimates. It is likely that such a constraint could not be imposed on some operational phases so that a real time recursive update of $\overline{K}_I$ could not always be possible when very fast mirror shape corrections must be imposed. For such cases a pre-operational training phase will be required and no attempt should be made to update the feedforward matrix with too noisy and not completely settled positions and forces, as that could destroy any good estimate already available. However, to allow maximum operational flexibility, the least square identification is solved with a recursive technique anyhow so that the choice of using just a pre-operational or a continuous identification can be made at due time, according to the requirements of specific observations.

In this way at the end of any set of independent commanded shapes the supervisor computer in charge of sending to the mirror the correct shapes to the decentralized DSP controllers receives from them the average positions and forces, so that at each instant of time the following equation can be written:

$$\bar{F}_k = \overline{K}_I \bar{p}_k + F_0 \tag{85}$$

F_0 being any constant or slowly varying external disturbing force, e.g. the mirror weight, the satellite attitude control couple, a local perturbation associated to variation of the environment temperature. Clearly for slowly varying forces the identification procedure must be applied recursively on line, as it will be explained later on. By taking its transpose, to set the unknown terms to the right, equation 85 is rewritten:

$$\bar{p}_k^T \overline{K}_I^T + F_0^T = \bar{F}_k^T \tag{86}$$

and condensed in the form:

$$\begin{bmatrix} \bar{p}_k^T & 1 \end{bmatrix} \begin{bmatrix} \overline{K}_I & F_0 \end{bmatrix}^T = \bar{F}_k^T \tag{87}$$

The least squares system clearly derives from stacking many of such equations to write:

$$\begin{bmatrix} \bar{p}_1^T & 1 \\ \bar{p}_2^T & 1 \\ \vdots & \vdots \\ \bar{p}_n^T & 1 \end{bmatrix} \begin{bmatrix} \overline{K}_I F_0 \end{bmatrix}^T = \begin{bmatrix} \bar{F}_1^T \\ \bar{F}_2^T \\ \vdots \\ \bar{F}_n^T \end{bmatrix} \tag{88}$$

that can be expressed as:

$$A\tilde{K}_I = B \tag{89}$$

with

$$A = \begin{bmatrix} \bar{p}_1^T & 1 \\ \bar{p}_2^T & 1 \\ \vdots & \vdots \\ \bar{p}_n^T & 1 \end{bmatrix} \quad , \quad B = \begin{bmatrix} \bar{F}_1^T \\ \bar{F}_2^T \\ \vdots \\ \bar{F}_n^T \end{bmatrix} \quad , \quad \tilde{K}_I = \begin{bmatrix} \overline{K}_I F_0 \end{bmatrix}^T$$

Once a sufficient number, i.e. $n \geq n_{act}$, of equations are available a first least squares solution of the normal system can be carried out in the form:

$$\tilde{K}_I = (A^T A)^{-1} A^T B \tag{90}$$

By calling $Z = A^T B$ and computing the LDL factorization $A^T A = LDL^T$, the above equation is rewritten as:

$$LDL^T \tilde{K}_I = Z \tag{91}$$

and $\tilde{K}_I$ obtained by a forward backward substitution of its LDL factorization factors on Z. Once $\tilde{K}_I$ is obtained its rows are sent to the corresponding DSP so that it can start computing the dot product with its measured positions to determine the feedforward force to be applied at its control point. This phase is what has been previously called the training phase and must clearly be based on a set of $n \geq n_{act}$ independent shapes commands. From this point onward a continuous updating of Z by

$$Z_{k+1} = Z_k + \bar{F}_{k+1} \bar{p}_{k+1}^T \tag{92}$$

and of the LDL factorization

$$R_{k+1} = R_k + \bar{p}_{k+1} \bar{p}_{k+1}^T \tag{93}$$

can be done, if the shape command steps are long enough and $\tilde{K}_I$ can be determined at assigned instant and distributed to the DSPs to adapt to slowly changing operational conditions. If that is not the case one must content himself with the training phase. It is noted however that the training phase adopts a recursive update form started by assuming $\tilde{K} = \varepsilon I$, with ε of the order of 10^4, as the recursive LDL update unsure a better numerical conditioning with respect to the batch solution of the normal least squares equations. It is well known that a recursive QR technique could be used in place of the LDL approach. The latter has been preferred because it is believed to be the best compromise between the need of a good numerical conditioning and computational effectiveness and because it allows a continuous adaptation, with reasonable computational power at the supervisor computer, whenever that is possible.

When the number of actuators reaches high values, the numerical simulation of the pre-operational identification phase can became too expensive in terms of computational time. For this reason the program allows to choose an alternative way to simulate the identification process, based on static response calculation. In fact once the system reaches the steady state position it is possible to neglect the time dependent terms and during the pre-operational phase feedforward contribution is null. So the global acting force can be written as:

$$\bar{F} = [K_P](p^{req} - \bar{p}) + F_0 \tag{94}$$

and it is possible to write the modal static equations describing steady behavior as:

$$[\omega_l^2]\bar{q}_l = X_l^T \bar{F} \tag{95}$$

One should note that we are considering a modal base without the free motions here, so the satellite is supposed fixed in the space and the modal stiffness is not singular. This means that we cannot evaluate the possible effect of the attitude control system directly because we should integrate the free motions to know the attitude control couple. But as we will report later, we can introduce noises on forces and positions to take into account the presence of disturbances linked to the satellite attitude controller. The system output can be expressed in two different manners, depending on the need of either employing high frequency residualization or not:

$$p = X_l q_l \qquad \text{without residualization} \tag{96}$$

$$p = X_l q_l + \left(\overline{K}^{-1} - X_l [\omega_l^2]^{-1} X_l^T\right) F \qquad \text{with residualization} \tag{97}$$

In the previous relations, without loss of generality, we have considered $p \simeq S = X_l q_l$ to simplify the writing of the equations. Now, combining equations 94, 95 and 97 or 96 into a single system, it is possible to find the steady force and position that will be achieved for a given command p^{req}. It is remarked that the system is not able to reach the commanded position because during pre-operational phase no information on the stiffness matrix is available yet and we are working without any feedforward contribution. The final system is:

$$\begin{cases} [\omega_l^2]\bar{q}_l = X_l^T \bar{F} \\ \bar{F} = [K_P](p^{req} - \bar{p}) + F_0 \\ \bar{p} = X_l \bar{q}_l \end{cases} \quad \text{or} \quad \begin{cases} [\omega_l^2]\bar{q}_l = X_l^T \bar{F} \\ \bar{F} = [K_P](p^{req} - \bar{p}) + F_0 \\ \bar{p} = X_l \bar{q}_l + \left(\overline{K}^{-1} - X_l[\omega_l^2]^{-1} X_l^T\right) \bar{F} \end{cases} \tag{98}$$

Putting the first equation of the system in the third and then substituting the force term $\bar{F}$ with the second equation we can obtain the final system for both cases:

$$(I + \overline{K}^{-1}[K_P])\bar{p} = \overline{K}^{-1}([K_P]p^{req} + F_0) \qquad \text{with residualization} \tag{99}$$

$$(I + X_l[\omega_l^2]^{-1} X_l^T [K_P])\bar{p} = X_l[\omega_l^2]^{-1} X_l^T([K_P]p^{req} + F_0) \quad \text{without residualization} \tag{100}$$

The system is solved with an LU factorization, using the GSL library, done only once at the beginning of the identification process. In this way the steady final position at each step is obtained by calculating the right hand side of equations 100 or 99, and by a forward/backward substitution to solve the system

$$[LU]\bar{p} = B \tag{101}$$

At the end it is possible to recover the force $\bar{F}$ by simply substituting the obtained position $\bar{p}$ in equation 94. To simulate a realistic experimental identification it is necessary to introduce appropriate noises and errors on the steady forces and positions. A good procedure has proven to be the following one:

- perform a sufficiently long simulation (a few times the command step length) with a constant requested position and without the feedforward term (because we have no stiffness matrix yet). The simulation has to be done with realistic actuators and sensors noises, correct quantization errors, and attitude control system switched on.
- extract from previous simulations forces and positions standard deviations (σ) over the time the system has been in steady state.
- use the force and position standard deviation just found to perform the following operation over each steady force an position values obtained through static response identification:

$$\bar{p}_{real} = \frac{\sum_{i=1}^{n}(\bar{p} + err(\sigma_p))}{n} \qquad \bar{F}_{real} = \frac{\sum_{i=1}^{n}(\bar{F} + err(\sigma_F))}{n} \tag{102}$$

  where n is the number of force and position values over which it is possible to do the average. So n depends on the command step time dt_{cmd} used during identification, control frequency ω_c, and controller performances in achieving the final steady position ($y\%(dt_{cmd})$):

$$n = (1 - y\%(dt_{cmd}))\, dt_{cmd}\, \omega_c \tag{103}$$

Figure 7(a) shows the comparison between the diagonal element of two stiffness matrices identified through the simulation and the static response approach. In figure 7(b) there is the comparison

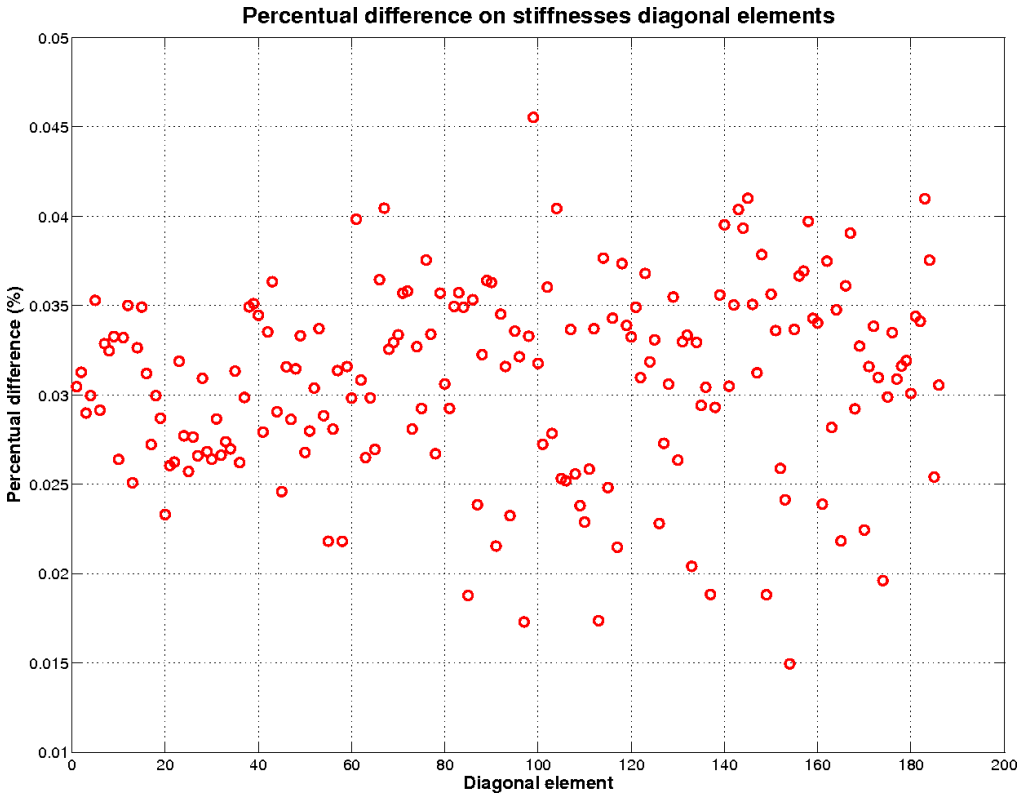

(a) Comparison between diagonal elements of two stiffness matrices identified through different approaches.

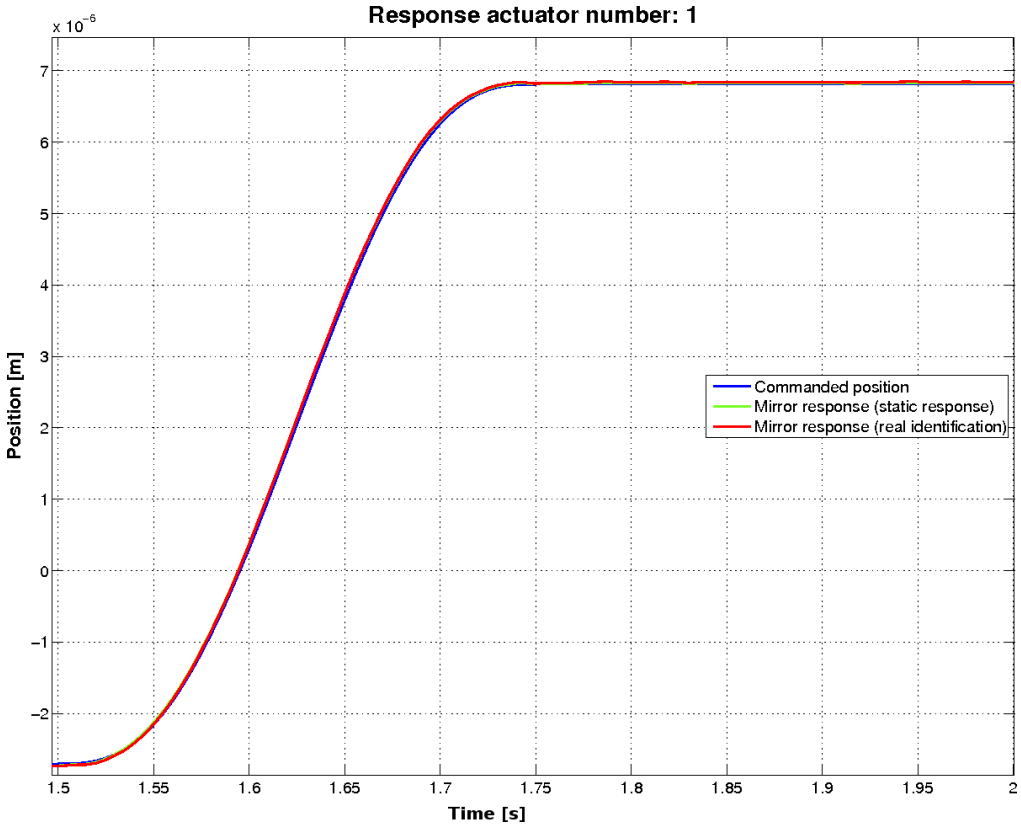

(b) Comparison between two system responses where the feedforward is based on different identified stiffness matrices.

Figure 7: Real simulation of identification process vs static response approach.

between two system responses using the feedforward contribution, based on the previous two differently identified stiffnesses. Both figures demonstrate that the static response approach can give a stiffness matrix equivalent to that obtained through the simulation of the real identification process. The advantage in calculation time is very important, for example to perform the matrix identification on a single PC through the real simulation of the identification process we need about 12 hours, while the static response approach can give an equivalent result in less than 5 minutes.

The main reason for the need of a precisely identified stiffness matrix is the lack of system damping and the constraint on the maximum controller feedback frequency. Low damping brings to low PD2 gains because of the presence of stability constraint, and low PD2 gains do not permit to help the feedforward action, from a static point of view, in reaching the requested position. Moreover if there is low damping it is very difficult to use sub-stepping technique because of the transient phase duration, that does not allow enough time for position and force averaging. So a system with low damping needs a quite precise identified stiffness matrix to assure the requested precision. This is clear our case in space where we can exploit system passive structural damping only while controller damping cannot add too much because of the constraint on the controller frequency.

The quality of the stiffness identification is primarily related to actuators and sensors noises and to quantization errors. Obviously a fundamental requirement is the ability of the controller to reach a steady state position in a given time. All these aspects are important in determining the pre-operational identification time. In fact if we have high noises and/or quantization error mated with a not so high active damping the only way to improve the stiffness identification is to increase the command step length, the command steps number or both. All these solutions tend to lengthen the time required for the identification process. Another possible improvement of the identification process can come from the use of optimized commands having a high force-position to noise ratio, obtained by imposing relatively high but feasible forces on each actuator. The related procedure is the following:

- choose the force vector in the requested range

$$\|\bar{F}_{range}\| = F_{min} \leq \bar{F} \geq F_{max} \tag{104}$$

- recover the related modal amplitude:

$$\bar{q}_l = [\omega_l^2]^{-1} X_l^T \bar{F}_{range} \tag{105}$$

- write the requested force as:

$$\bar{F}_{range} = [K_P](p^{req} - p) + F_0 = [K_P](p^{req} - X_l \bar{q}_l) + F_0 \tag{106}$$

- substitute equation 105 in 106 and solve to obtain p^{req}:

$$p^{req} = [K_P]^{-1}(F_{range} - F_0) + X_l[\omega^2]^{-1} X_l^T F_{range} \tag{107}$$

where p^{req} represent the vector of commanded positions we were looking for. In this way we impose forces values during identification, but there is the problem of positions too. In general is not possible to obtain both requested positions and forces, but in the LIDAR project the mirrors can do rigid motions, so we can apply a rigid shift to the positions recovered through equation 106, without changing the forces values. In this way we can control both the position-noise ratio and the force to noise ratio, thus improving the identification quality.

Command steps number n	3000
Command time length (dt_{cmd})	0.5 sec
Total identification time	25 min
Control frequency ω_c	4000 Hz
Position standard deviation σ_p	30e-9 m
Force standard deviation σ_f	1e-5 m
Quantization	16 bit
Actuator stroke	$\pm$0.0005 m
Actuator force range	$\pm$0.2 N

Table 3: Control parameters resume.

Once we have obtained the identified stiffness matrix we would like to know the error that has been introduced. This requires a reference stiffness matrix, which depends on the usage, or not, of the high frequencies residualization procedure. If we do not use any residualization the stiffness that we are identifying is (remember equation 22):

$$\overline{K}_{ref} = X_l[\omega_l^2]^{-1}X_l^T \tag{108}$$

Instead if we use the high frequencies recovery the reference stiffness matrix is simply the physical stiffness reduced to the scalar points obtained from FEM analysis:

$$\overline{K}_{ref} = \overline{K} \tag{109}$$

Figure 8(a) reports the percentage difference between diagonal elements of the reference stiffness and the identified one. This matrix identification has been performed using 3000 commanded steps, with a step duration of 0.5 s, corresponding to an actual testing time of 25 minutes. The fundamental parameters used are resumed in table 3. Figure 8(b) shows the percentage error of extra-diagonal matrix elements. Here significantly worse errors show up but they refer to approximately null elements linked to the low stiffness coupling between petals and central mirrors.

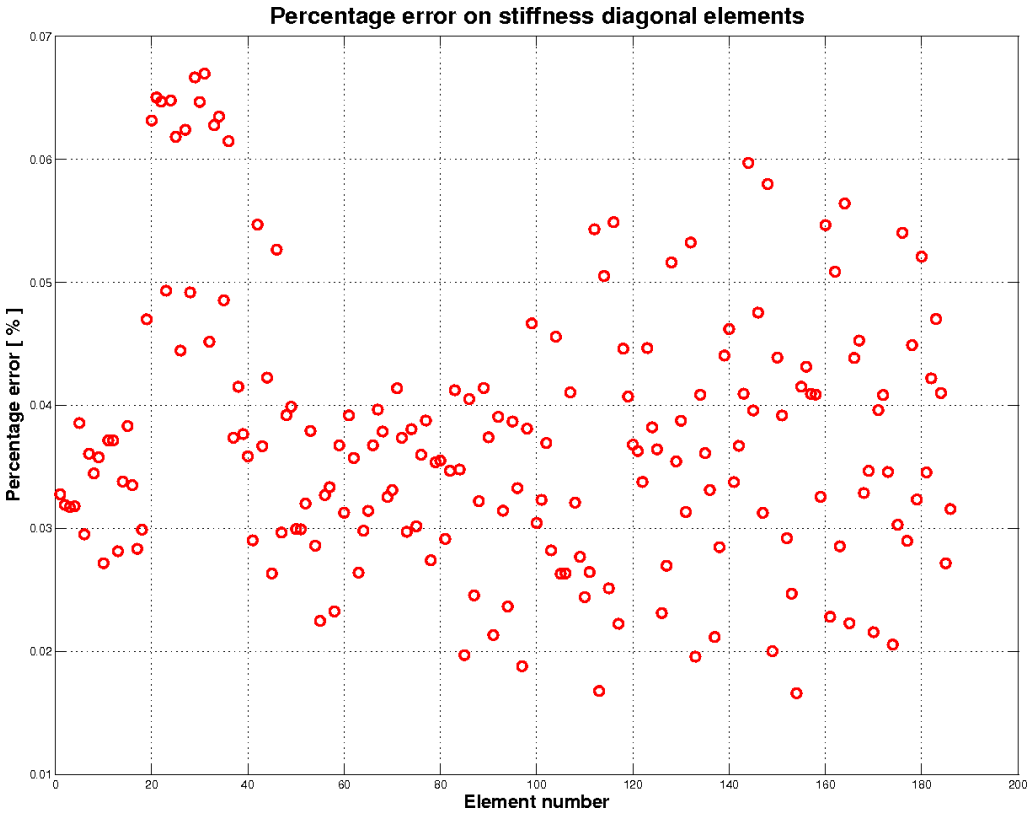

(a) Diagonal elements.

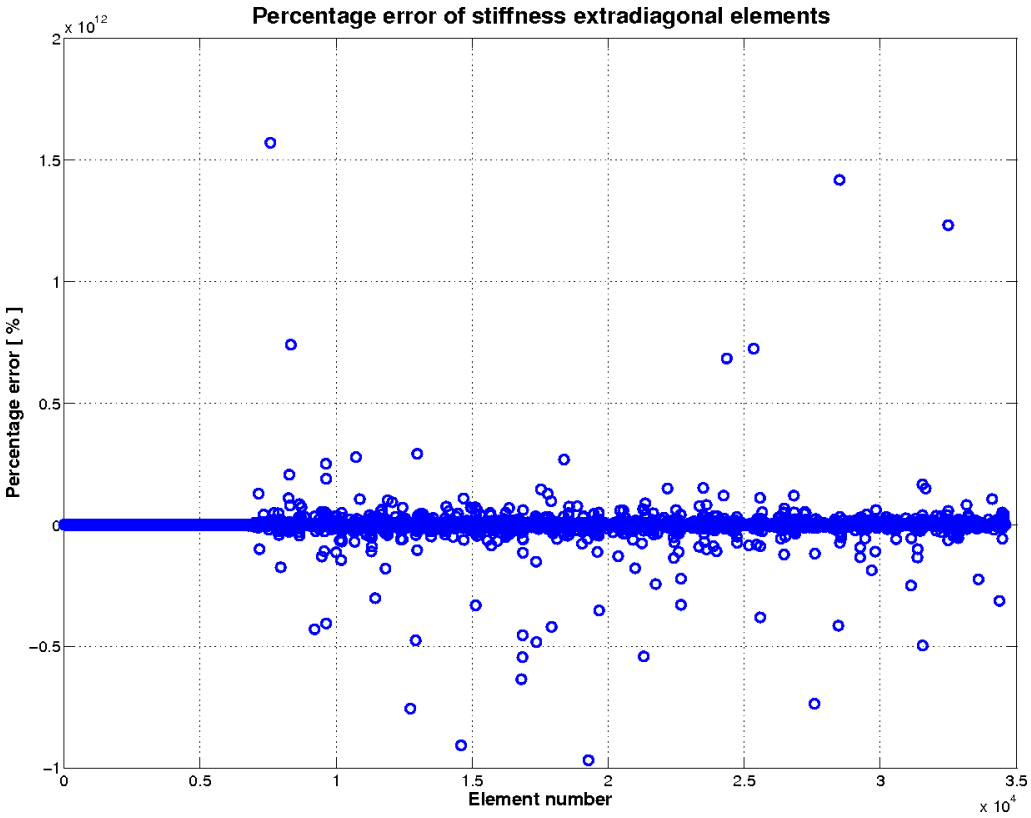

(b) Extradiagonal elements.

Figure 8: Percentage error of identified stiffness elements.

10 Secondary mirror

The secondary mirror is mounted at the top of a spike that is about 3 meters high. Its role is to reflect the light captured by the primary mirror to the sensor that acquires the image informations, see figure 9. We are interested to know the range of the secondary mirror displacements caused by excitations coming from the adaptive controller of the active primary mirror, to verify if it can compromise telescope performances. In particular we have analyzed possible losses of the line of sight of the center of the secondary mirror from the ideal position and we have evaluated the secondary mirror plane tilt. In this way we have been able to compute where a line normal to secondary mirror plane intersect the sensor plane, about 3 meters below. The sketches reported in figures 10(a) and 10(b) summarize the procedure described below. The three red points of figure 10(a) are coincident with the three structural FEM nodes positioned where the secondary mirror is connected to the spike. The green point corresponds to the FEM node that is placed at the sensor position. From the simulation code we can evaluate the global displacements of these points by simply putting the relative FEM nodes degrees of freedom inside the initial scalar points set, in the same way followed to obtain the satellite free rotations. The blue point represents the center of secondary mirror; we can always find its position because it is located in the center of mass of the triangle. Once we know these informations we can recover the deformed positions of the three points describing the borders of the secondary mirror and so the displaced position of the secondary mirror center of mass. Through the three points of the triangle we know the secondary mirror deformed plane too, so we can recover the normal vector to the plane. It is now possible to find where the projection along the normal line intersect the sensor plane. The sensor plane tilt rotations are considered rigid, while its translations are taken into account, and are assumed to be equal to the sensor point displacements. In this manner we can know the alignment error between the center of the secondary mirror and the sensor, evaluate the effect of the secondary mirror plane deformation, and ultimately determine the precision of optic reflections.

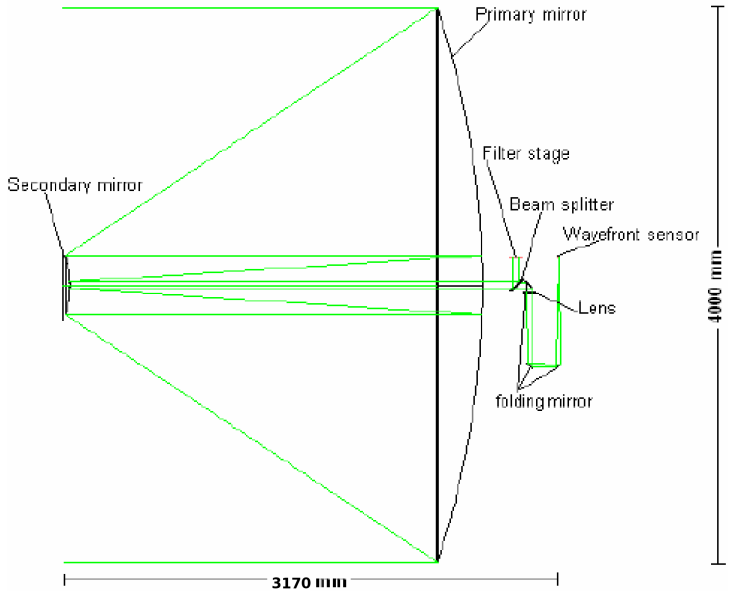

Figure 9: Sketch of the optical configuration (Credit by Carlo Gavazzi Space).

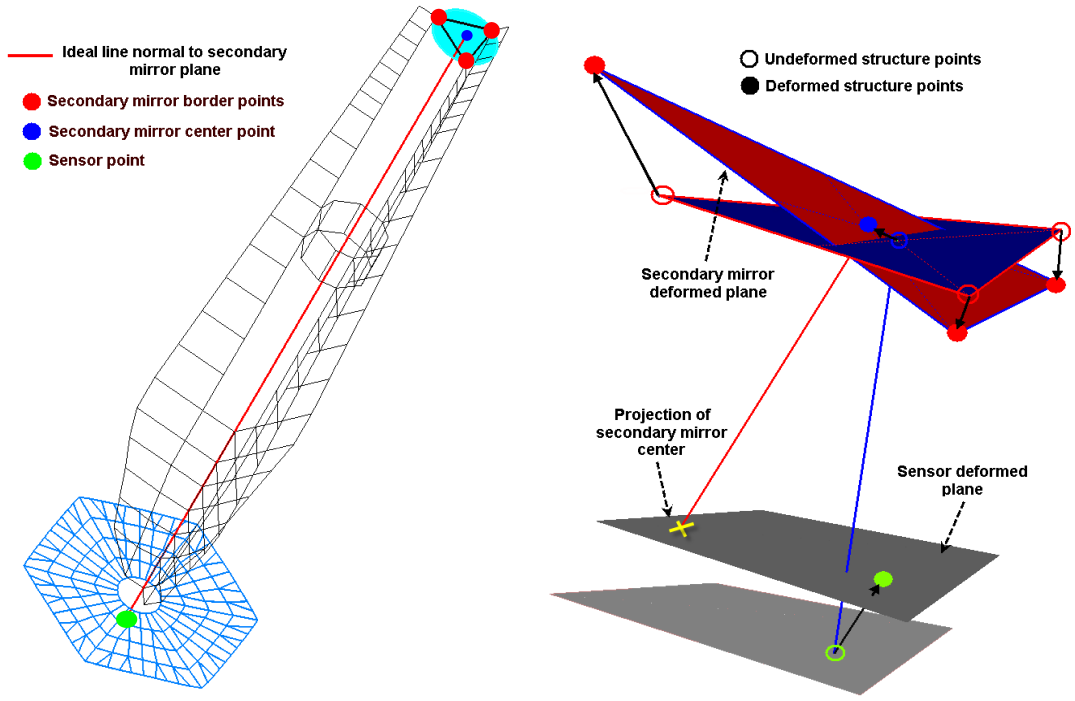

(a) Spike, secondary mirror and sensor.

(b) Procedure description.

Figure 10: Satellite secondary mirror displacements recovery.

11 Simulation results

All the following results have been obtained with a 4000 Hz mirror control frequency, using the parameters reported in table 2. The controller requested precision at the end of each command step is ±200E-9 m. The attitude control system has always been switched on using the setting parameters reported in table 1.

The first simulation (figure 11) shows the system response to a simple step, in order to verify that the control system is able to reach the commanded position and to prove a stable behavior.

Figures 13, 14 and 15 report the simulation results of a random commanded history characterized by small deformations, in the order of ±2E-6 m (see figure 12). This history underlines the low precision due to quantization errors of forces and, especially, positions. In fact the position resolution is 15 nm, a value that is higher than the average gap reported in the zoomed window (figure 13). Moreover the PD2 action is strongly determined by sensor noise. Considering the entity of quantization and noise errors the control actually acts in a bang-bang manner, which maintains the mirror response within a range of ±30E-9 m around the commanded position. Figure 14 shows the difference between the orders of magnitude of feedforward and PD2 contributions. As we have already underlined, the PD2 gains must be kept low because of stability constraint linked to low passive damping and low control frequency. In figure 15 it is possible to note that in this simulation the maximum force value is below the saturation limit of 0.2 N. Figure 16 reports the secondary mirror center displacements from the ideal position aligned with the sensor. Figure 17 shows the secondary mirror center projection on the sensor plane to underline the effect of the secondary mirror surface rotation. The red circle frames all the displacements while the green one encloses the displacements measured at the end of each command step. In this case the order of magnitude of the displacements magnitude is always below 10 nm. In this section there are no figures giving

informations about the out of plane displacement of the secondary mirror because it is always very low (under 1 nm.) and so leads to no interesting data.

Figures 19 and 20 show a simulation with higher steps amplitude, the related displacements are here contained in the range ±25E-6 m. The commanded history is random so the required mirror's shape could be quite wavy as seen in figure 18. Anyway the control action assures the final correct mirror position with a precision in the order of $30 \div 80$E-9 m, as magnified in the zoomed view. In this case control forces reach values that are beyond the saturation level. Such values are surely affected by the random imposed deformation, moreover all the actuators connections with mirrors are described through 3D hinges and all the actuators directions are not perpendicular to the plane but parallel to satellite spin axis, so involving a high in-plane mirrors stiffness during deformation. This latter effect can increases the control forces especially at the actuators positioned on the external sides of petals, where the mirror-actuator angle can reach 18°. If we compare figure 20, related to a central mirror actuator force, to figure 21, related to an external actuator, we can appreciate an important difference in forces values. This implies that forces can be higher than the final real ones, but it is quite unlikely that with the current actuators density and power this kind of deformations could be achieved, even with the final correct configuration. Anyway this aspect should cared of along with the decision about the mirror-actuator connections. Figures 22 and 23 refer to secondary mirror displacements in a range of about 35 nm. The higher range respect the previous history is in accordance with the higher forces needed by the control system.

An important design specification is that the control system should be able to adjust the mirrors position after initial deployment trough relatively high rigid displacements. This is the main reason of the high measurement range imposed on displacement sensors (±0.0005 m). Figure 25 shows the simulation of a history based on rigid mirrors displacements, as seen in figure 24. The rigid motions are along the axial actuators direction because, with the actual mirrors-actuators connection, these are the only rigid movements allowed. The displacements are large, in the order of ±0.005 m, so that they are close to the limit imposed by the specification. It is possible to appreciate that the controller is able to reach the requested positions within the requested precision in the last 20% of the command step. As the zoomed view displays, the mirror response is not easily dumped by the control system, especially on petals control points. The main reason of that it is the coupling between high rigid motions displacements and low frequency modal forms, that have the least passive damping. In particular the first six petals modes are hardly observable and controllable. So, as we have already underlined in section 3, the previous petals modal forms must have a frequency of at least 20 Hz to achieve a satisfactory controller performance. This implies either a stiffer solution than that initially available or the possibility to add dampers to petals hinges. Figure 26 shows the controller performances with the first preliminary design data that was not able to satisfy the precision requirements; in the zoomed view it's clear the controller difficulty in damping the mirror response. Figure 27 shows the very low force level needed to control rigid motions that, once the steady state is reached, is mainly related to system noises and quantization errors. This is a proof that the initial fictitious axial stiffness used to remove rigid motions is really unimportant, and that the high frequencies residualization works correctly. Figures 28 and 29 show the secondary mirror displacements which reaches higher values in this case than in the previous ones. In fact the displacements magnitude order is around 300 nm with peaks of about 600 nm. This range growth is not linked to the forces values because, as we have just seen, the forces to control the mirrors rigid motions are very low. But we have also underlined that the rigid movements excite the petals modal shape, that have low damping and a frequency of 20 Hz. The spike mounting the secondary mirror on its top has a modal shape with a frequency of about 20 Hz too, so when the mirror controller excites the petals modal shapes we obtain as a consequence the spike excitation

that brings to higher secondary mirror displacements. If such a range of displacements is to be considered too high a possible solution could be a frequency separation between the modes of the petals hinges and the spike. It is important to underline that after the transient phase the range of displacements comes back to lower values, i.e. below 200 nm, as it is possible to see in figure 30. So if the mirrors during their operational life are not requested to perform high rigid jumps in a few seconds this will not cause any problem. Figure 31 refers to the same history just shown but with a command step frequency of 0.25 Hz, assuming a more realistic request for high rigid movements at a lower frequency. The image demonstrates that after the command step transient the secondary mirror displacements range decreases below 30 nm.

Figure 32 is related to a history where rigid motions are coupled to mirrors deformations, here to be more realistic the movements range has been set to ± 0.00025 m. In this case the requested tolerances are satisfied in the last 40% of command step.

Figure 33 shows a chess square deformation imposed on a petal mirror, where the amplitude range is $\pm$2.5E-6 m. This kind of shape does not represent a problem for the controller performance, as shown in figure 34, but it is one of the most critical from the force levels point of view. In fact in figure 35 we can see that even if the deformation range is not so wide the forces needed are highly over the saturation level.

Figure 36 reports the simulation of a time history that represents the first 100 modal shapes. This is a classical test to verify the controller effectiveness and it is here performed by imposing a wide deformation range of $\pm$50E-6 m. As it is possible to appreciate in the zoomed view the steady state position can be affected by an important gap due to stiffness matrix identification errors. Obviously the stiffness precision become more important when the deformation range grows up. Anyway in figure 37 the maximum error of each step of simulation is reported and it is evident that even with this high deformation range the requested precision is guaranteed once the response reaches steady state.

Figure 38 shows a comparison between two responses, with and without the presence of dynamic feedforward terms. These are important to improve the transient quality of each step, as magnified in the figure zooms.

As shown up to now the feedforward contribution is quite important, so a correct stiffness matrix identification is fundamental to obtain a good controller. Figure 39 reports the different control precision obtained with different stiffness matrices affected by different noise values during identification:

- "0 noise" is the ideal situation where the identification is performed without quantization errors and Gaussian noises;
- "1 noise" refers to 30E-9 range error on position and $1E-5$ range error on force, i.e. the ones used up to now;
- "2 noise" refers to 90E-9 range error on position and $3E-5$ range error on force;
- "3 noise" refers to 150E-9 range error on position and $5E-5$ range error on force;

All the identifications were performed trough the static response approach to minimize computational time. The commanded history implies a random wide range deformation of $\pm$100E-6 m to emphasize the identified stiffness effect on control precision. This simulation confirms the importance for this project of a good identification and so the relevant role of quantization errors and noises in determining controller performances. But as we have demonstrated in section 8, the application of sub-stepping technique to control action can allow high control precision even with

a roughly estimated stiffness matrix. Unfortunately we could not apply it because of poor dynamic control performances. Anyway to demonstrate the control capabilities we have set the control frequency to 10 KHz to obtain a very good dynamic behavior and we have performed the previous simulation using 3 sub-steps inside each main commanded position. The result is reported in figure 40 where it is possible to appreciate the large control precision improvement, that is partly due to higher PD2 gains and partly to sub-stepping application. Note in the zoomed view that at the end of commanded step the three responses converge to the same solution in spite of different stiffness matrices. This confirms the convergence demonstration carried out in section 8.

The results presentation ends with some images referred to the behavior of the attitude control system. Figures 41 and 42 show the ability of the attitude controller to maintain the null reference position of the satellite and the couple needed. Figures 43 and 44 show the capabilities of the controller to reach and maintain commanded attitude angles with the necessary couple; note in particular the actuators saturation. The last figure 45 makes a comparison between the same mirrors commanded history but with the attitude control switched on and off. The related responses prove that there is no significant interaction between the two controllers, even when the satellite is rotating under the couple imposed by the attitude control system.

It is finally important to remark that all simulations presented in this section have been performed with an A/D/A plus computational delay of half the sampling time, i.e. a very significant delay. This means that it is either possible to implement the controller with low computational power or to improve its performances if the available power is higher.

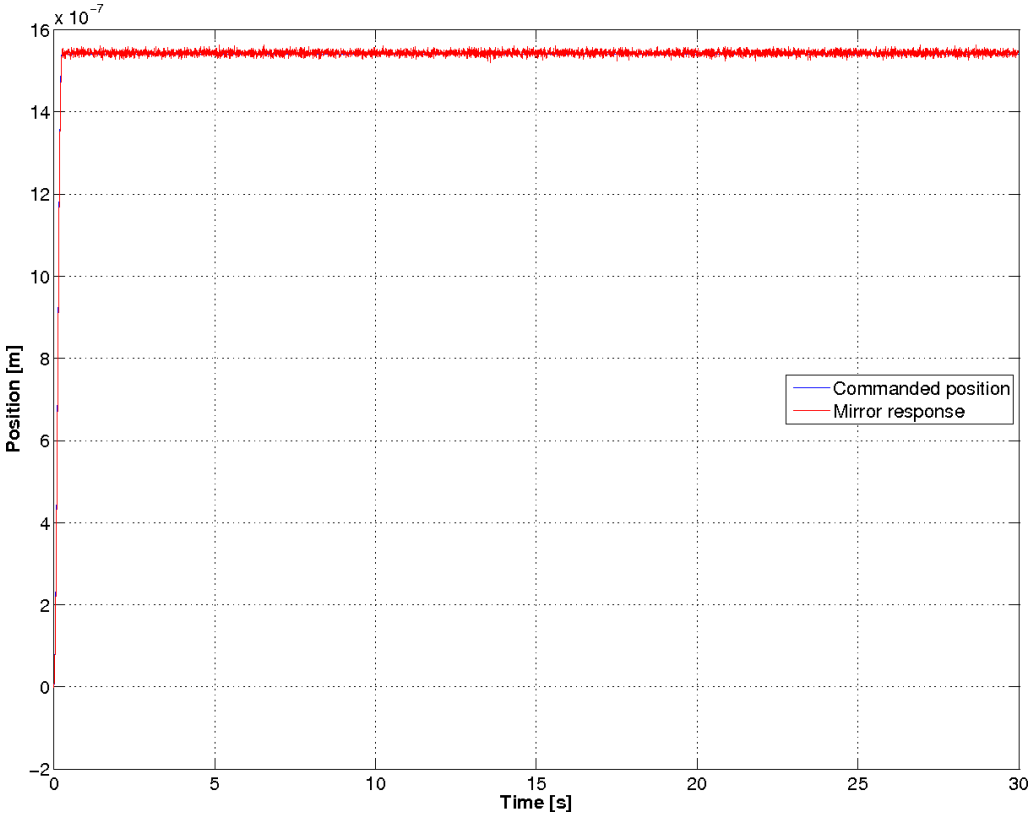

Figure 11: Step response, simulation 1.

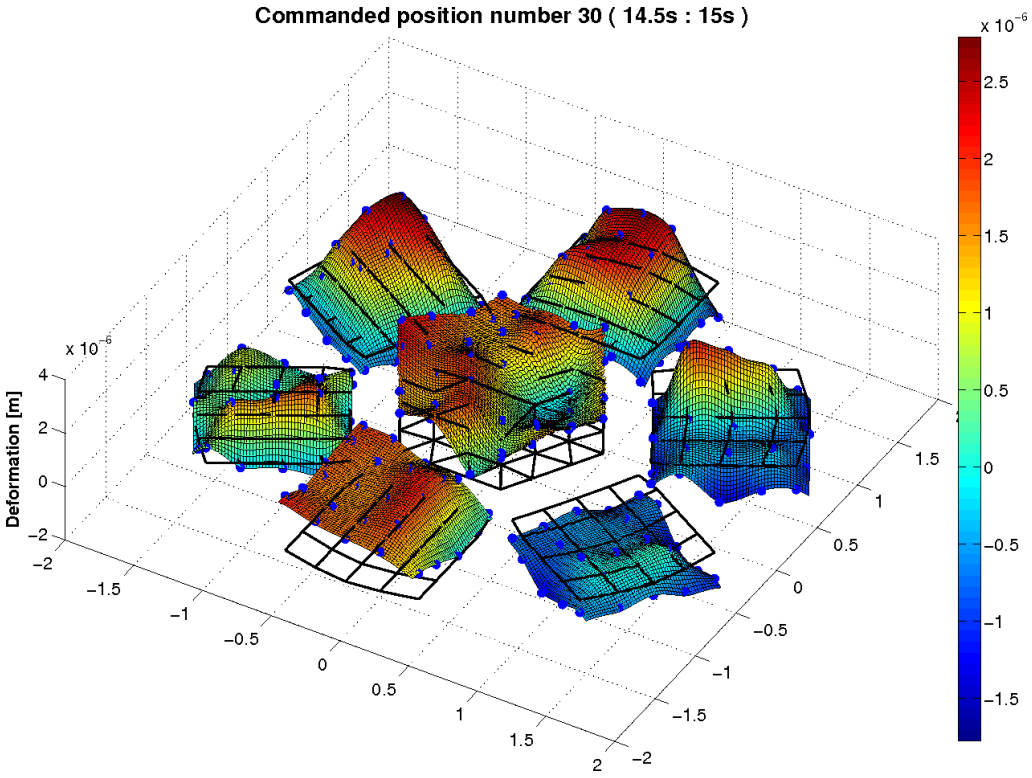

Figure 12: 3D mirror deformation of simulation 2.

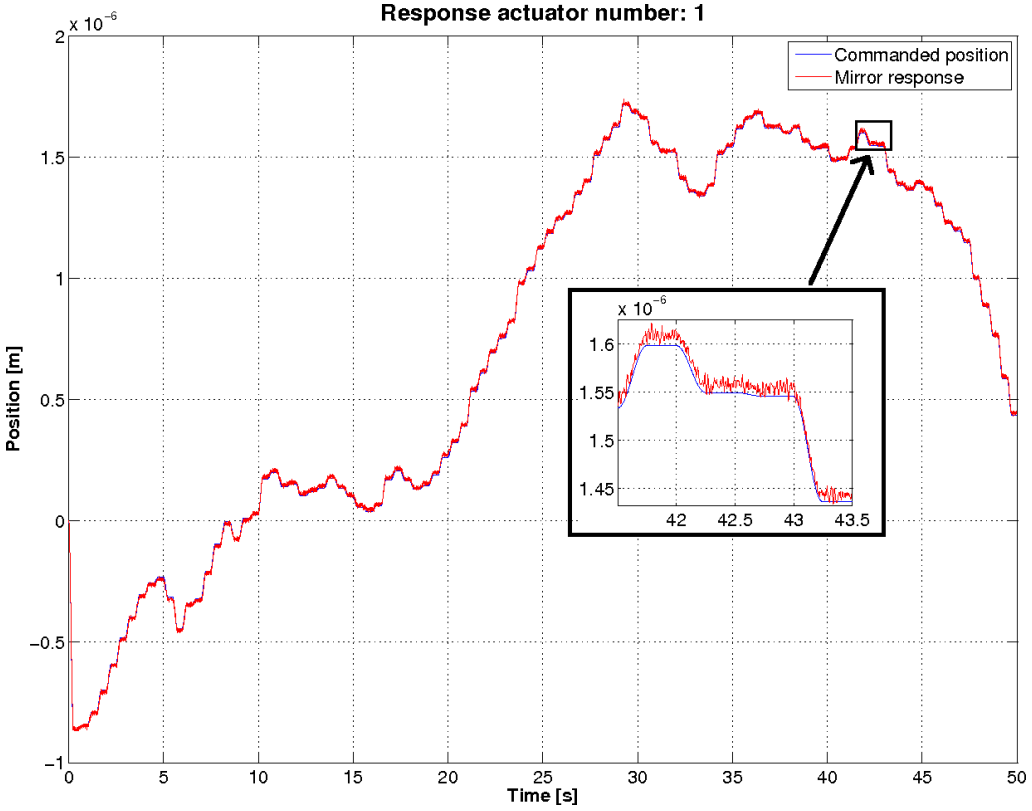

Figure 13: Response simulation 2.

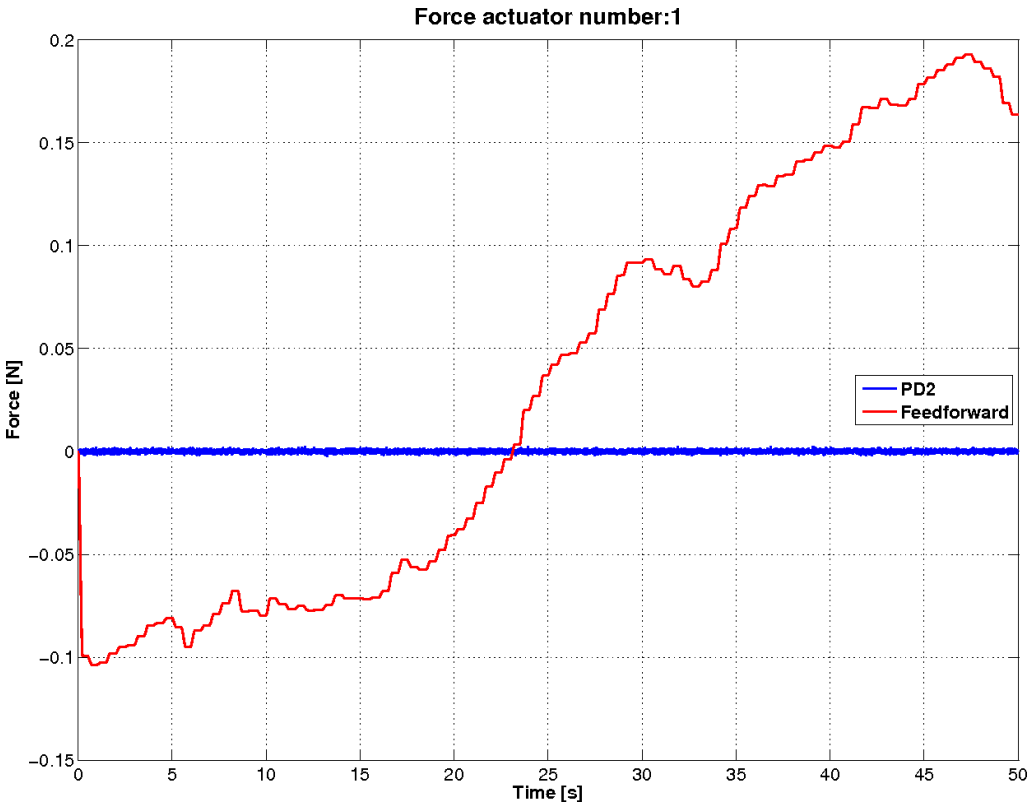

Figure 14: Feedforward and Pd2 force contributions of simulation 2.

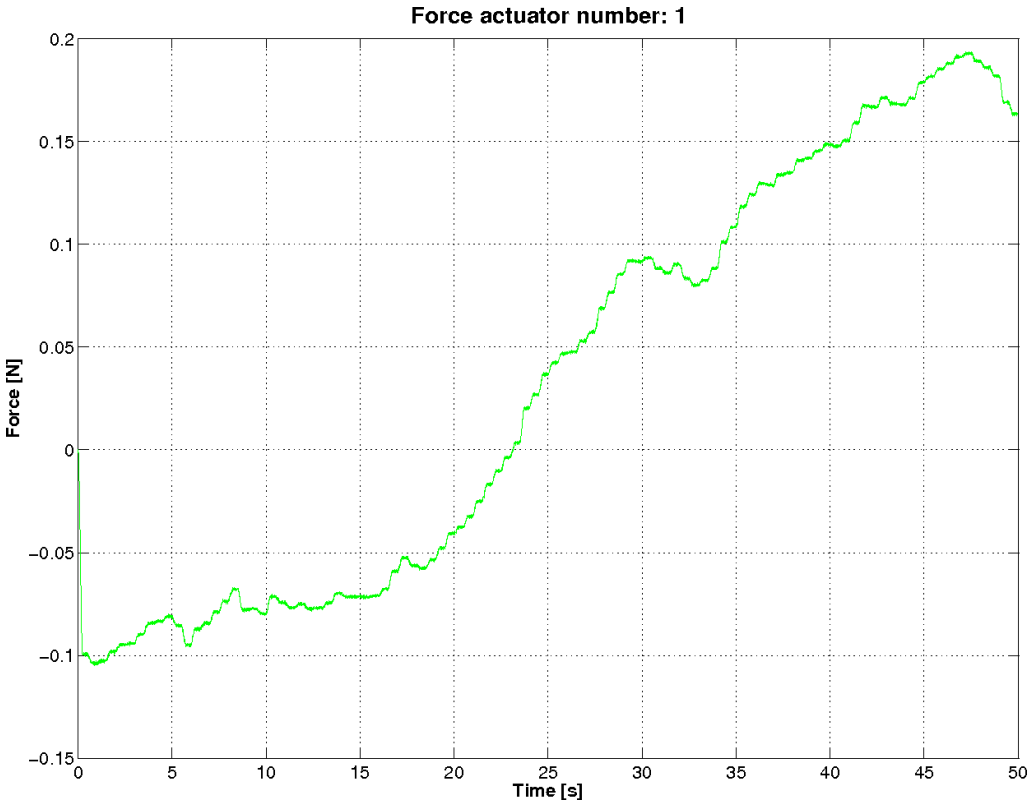

Figure 15: Control force of simulation 2.

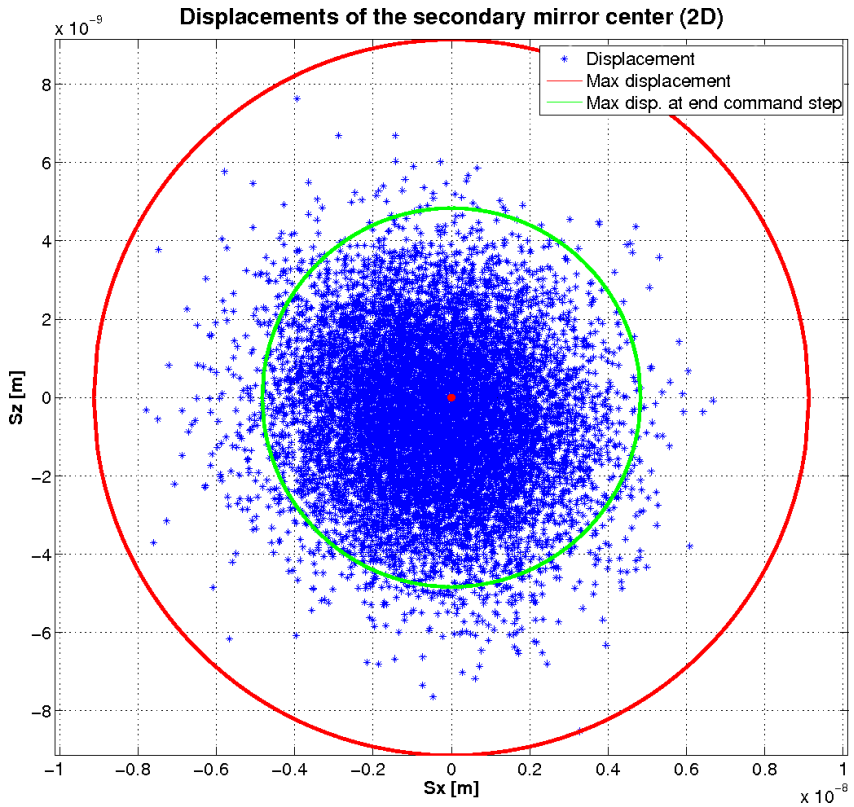

Figure 16: Secondary mirror center displacements, simulation 2.

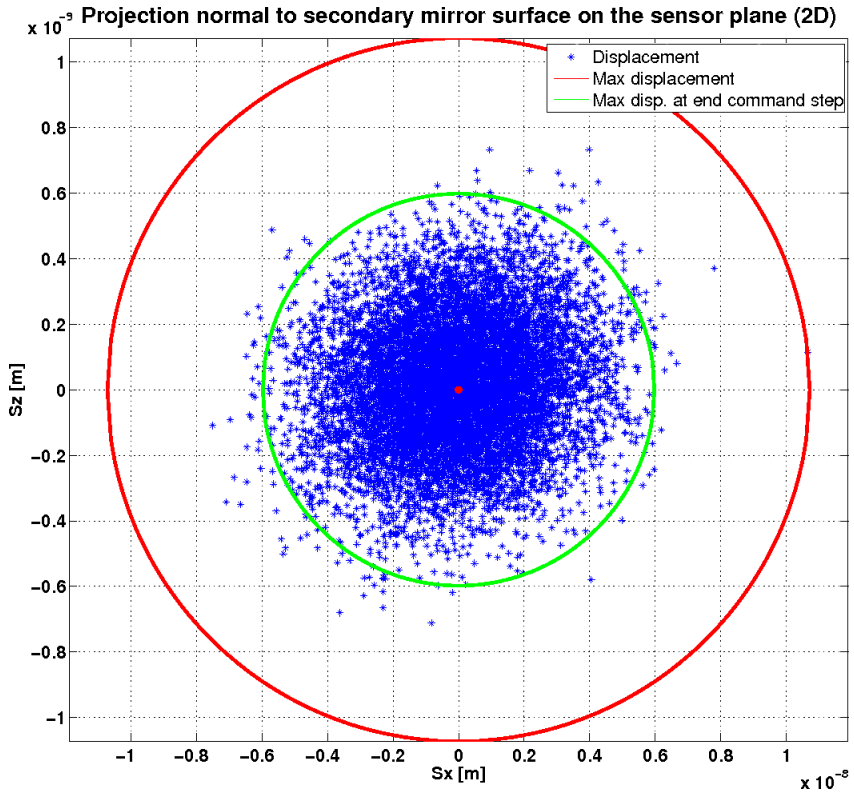

Figure 17: Secondary mirror center projection on sensor plane, simulation 2.

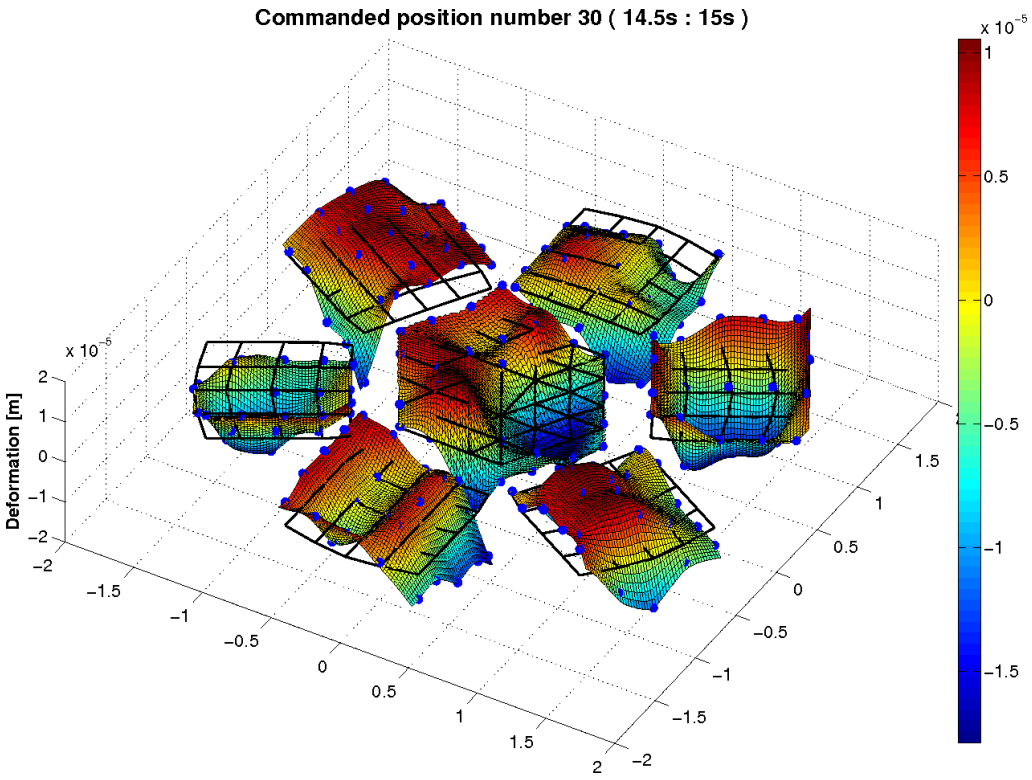

Figure 18: 3D mirror deformation of simulation 3.

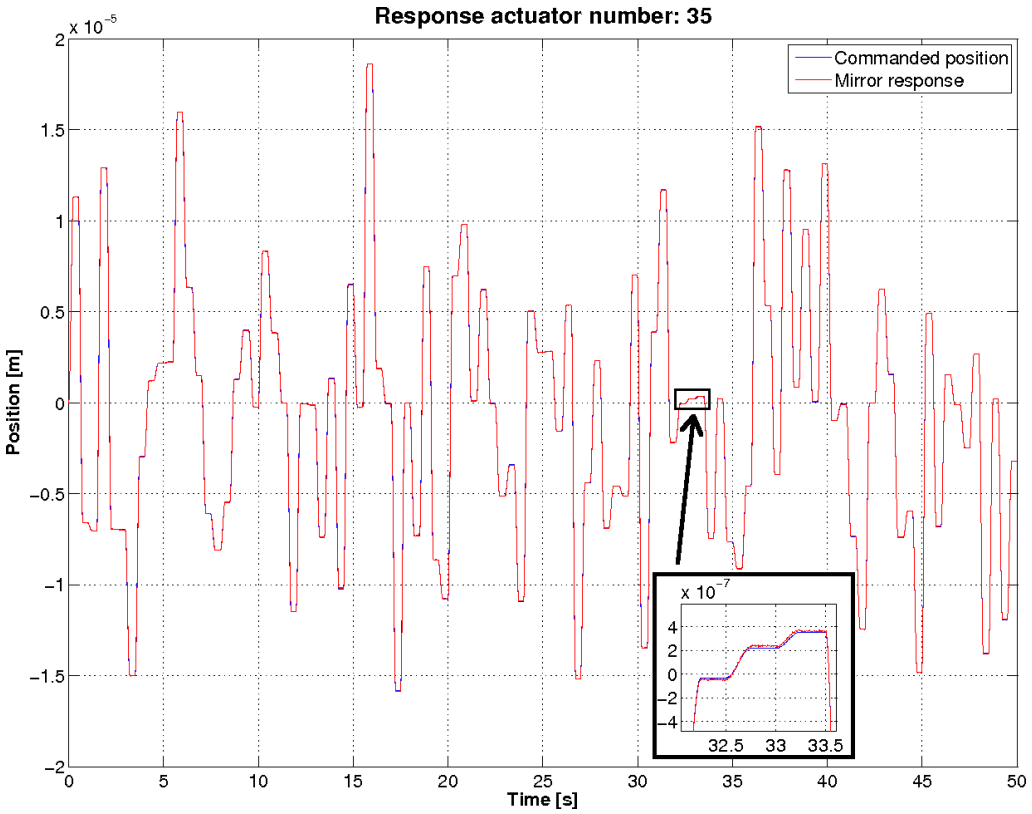

Figure 19: Response simulation 3.

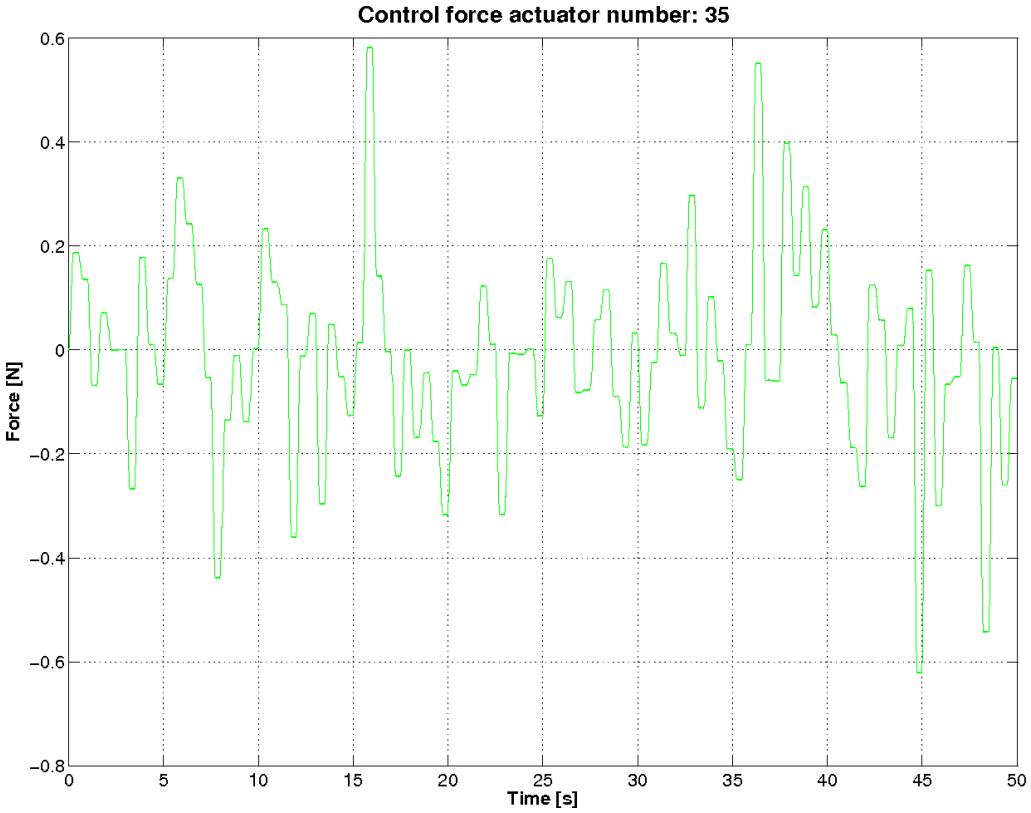

Figure 20: Control force of a central mirror actuator, simulation 3.

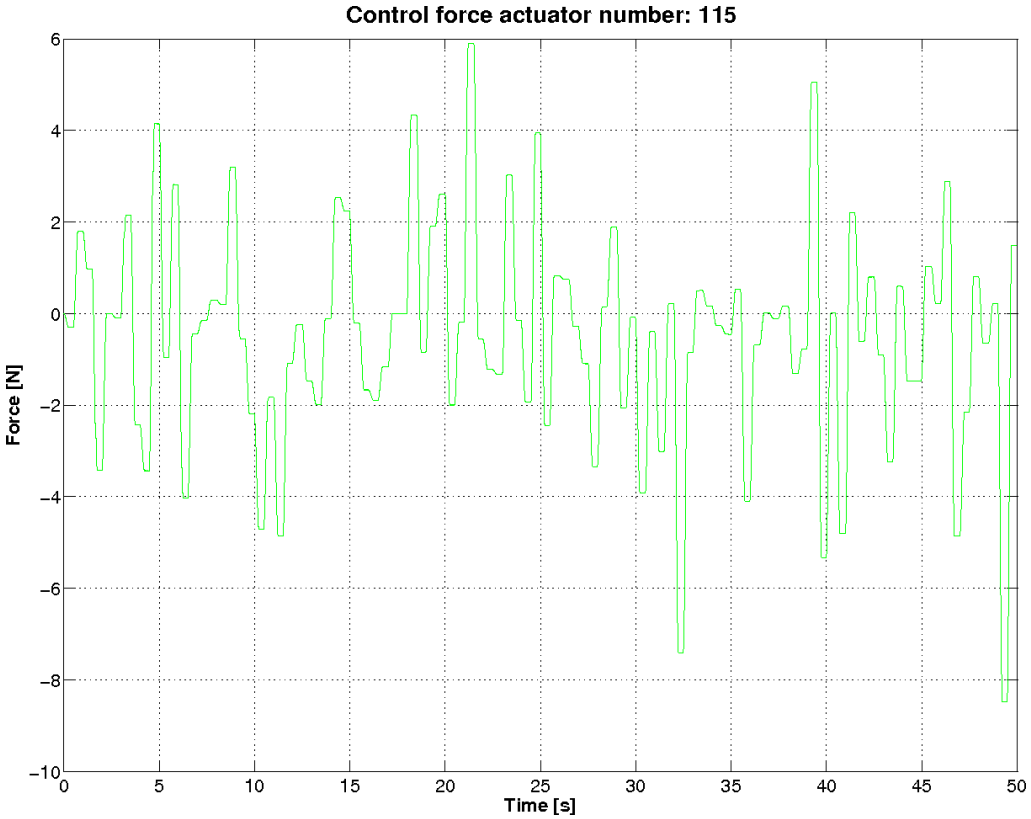

Figure 21: Control force of external actuator, simulation 3.

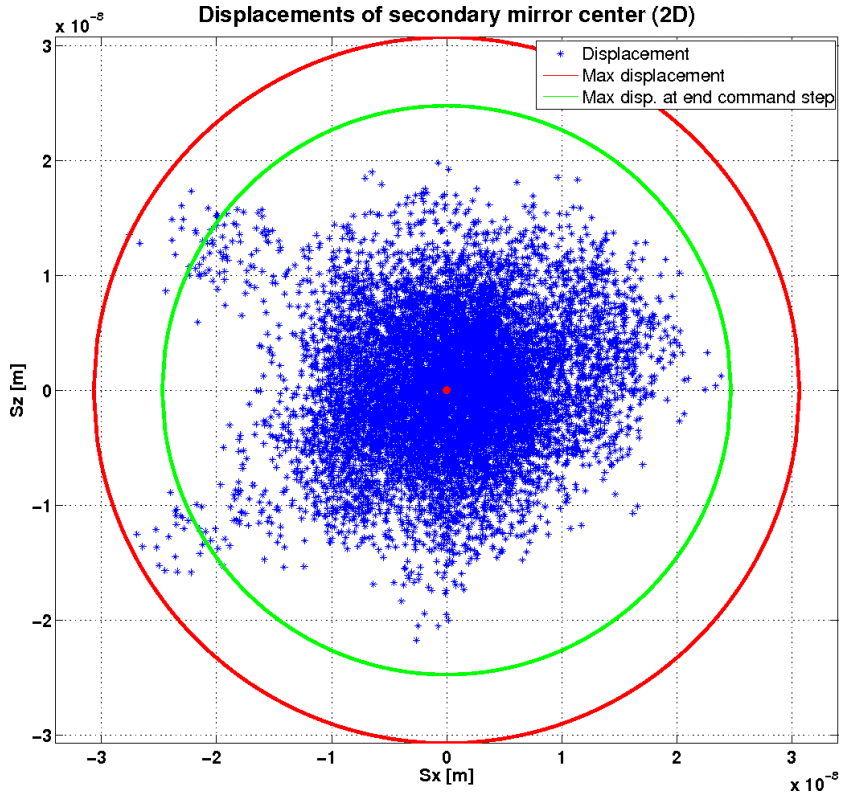

Figure 22: Secondary mirror center displacements, simulation 3.

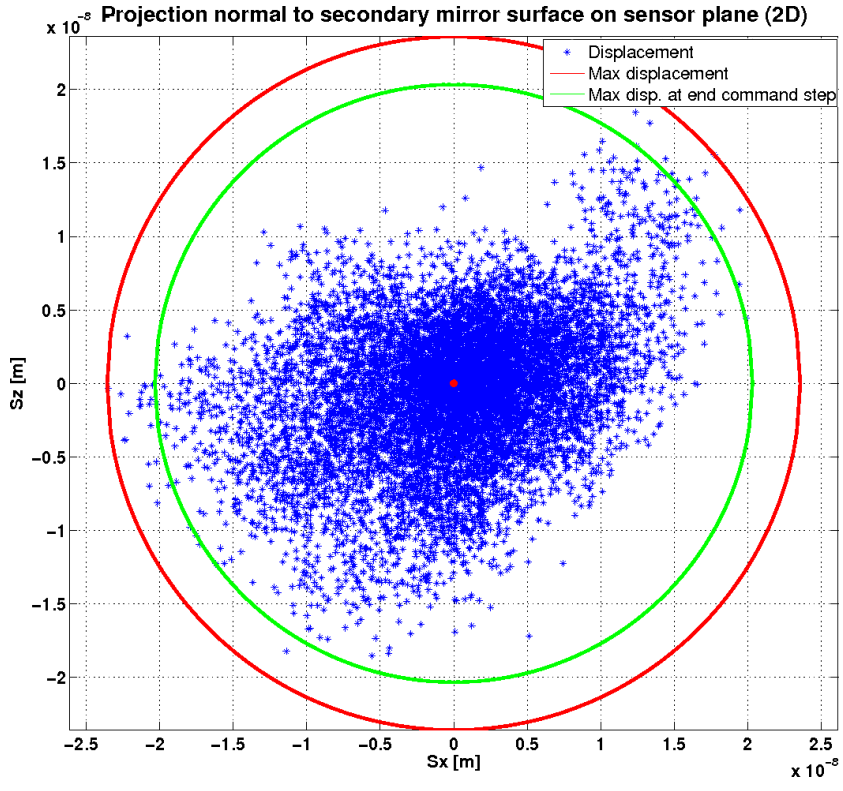

Figure 23: Secondary mirror center projection on sensor plane, simulation 3.

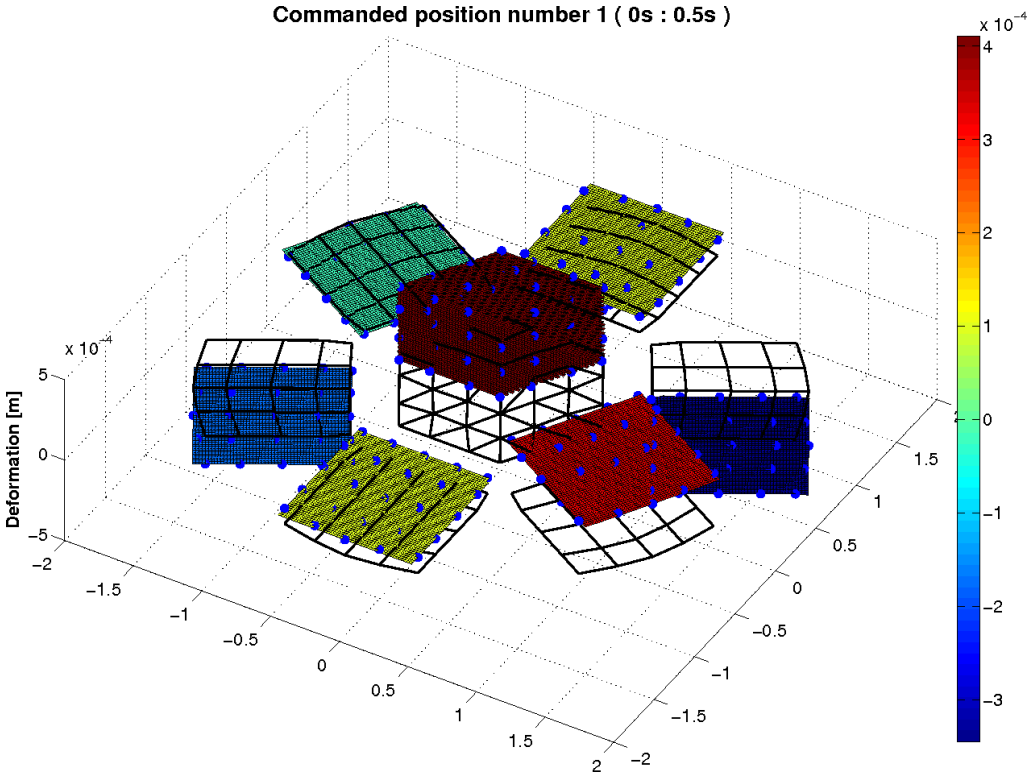

Figure 24: 3D mirror rigid motions, simulation 4.

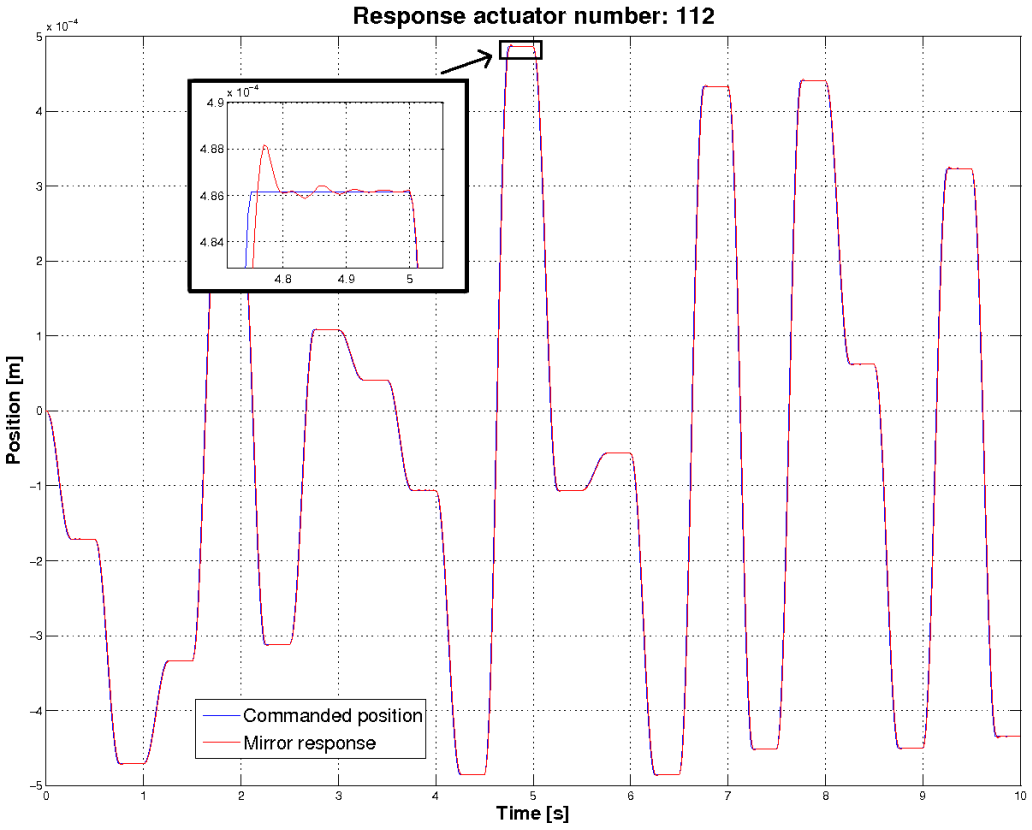

Figure 25: Rigid motions control, simulation 4.

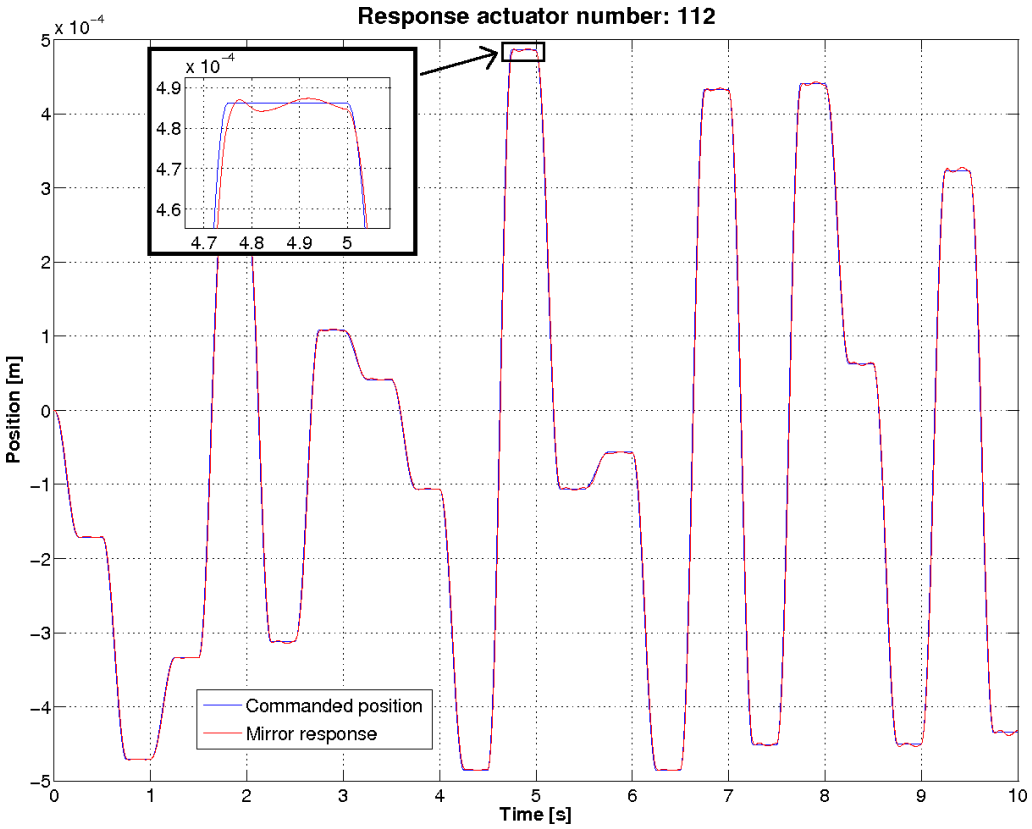

Figure 26: Rigid motions control with petals hinges modes with a frequency below 20 Hz, simulation 4.

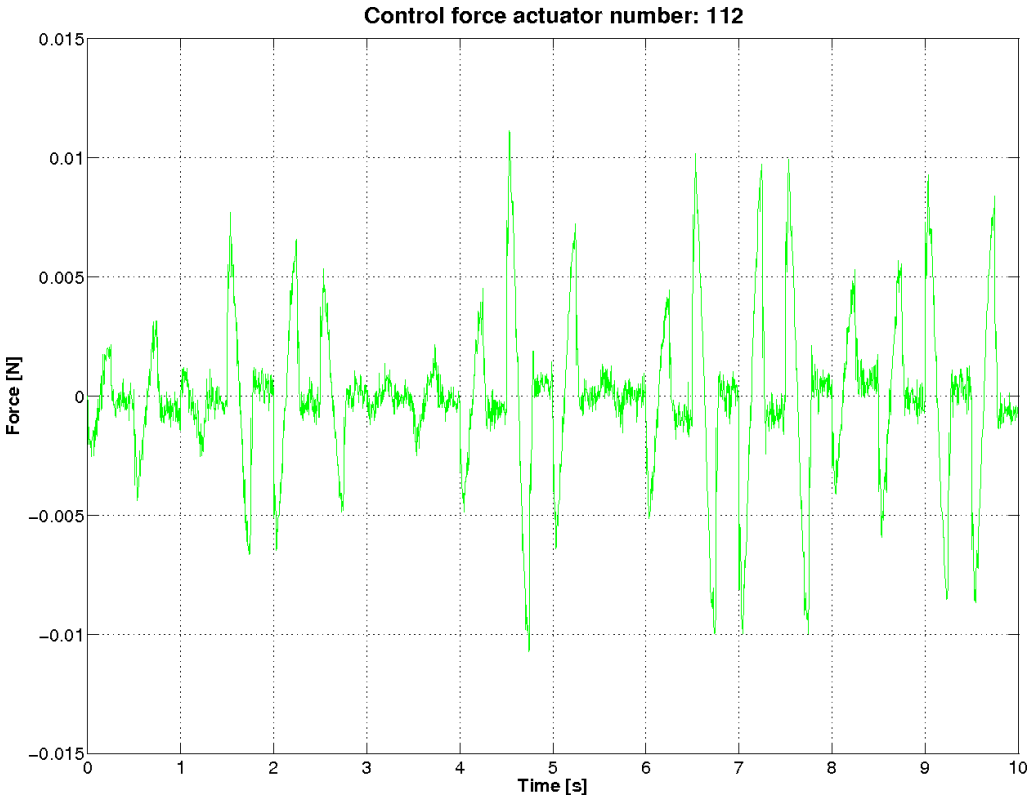

Figure 27: Rigid motions control with petals hinges modes with a frequency below 20 Hz, simulation 4.

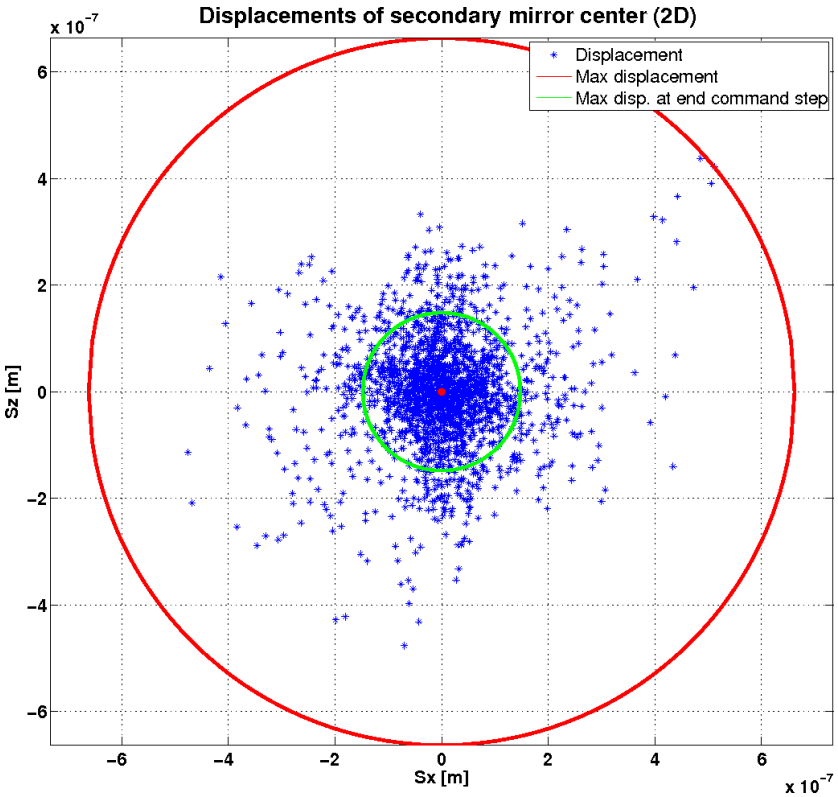

Figure 28: Secondary mirror center displacements, simulation 4.

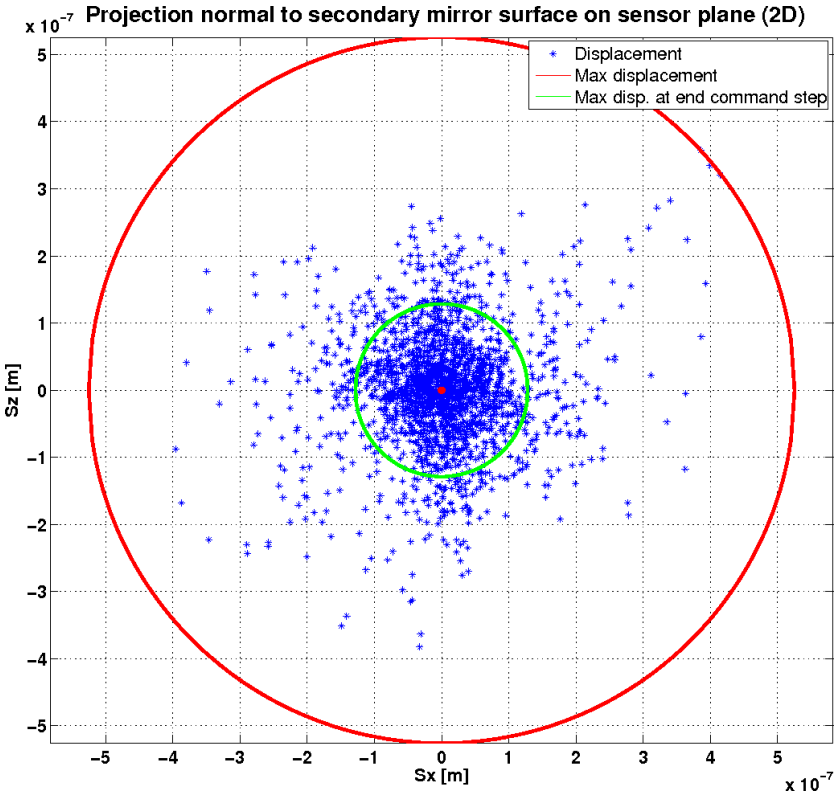

Figure 29: Secondary mirror center projection on sensor plane, simulation 4.

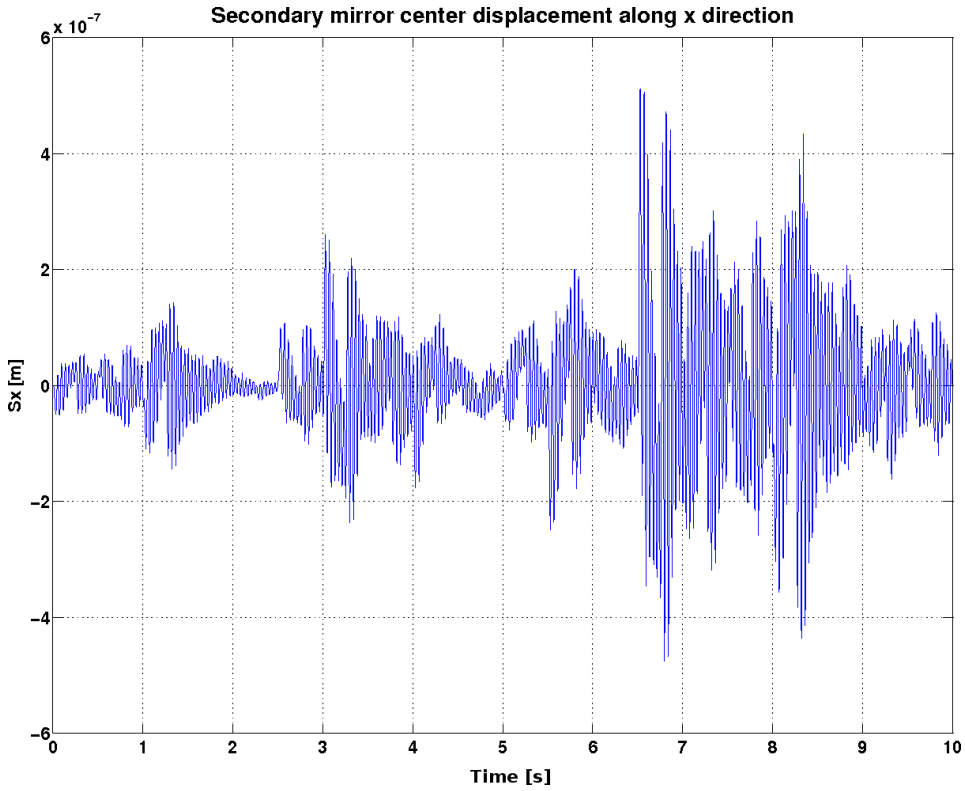

Figure 30: Secondary mirror center displacement along x direction, simulation 4.

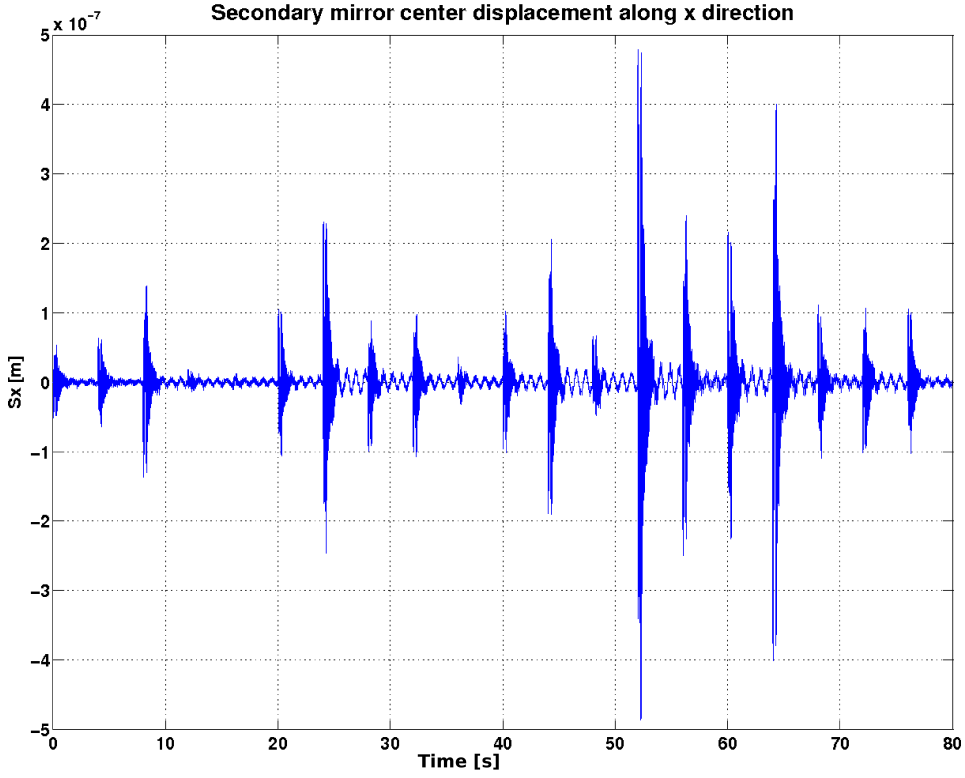

Figure 31: Secondary mirror center displacement along x direction with a command step frequency of 0.25 Hz, simulation 4.

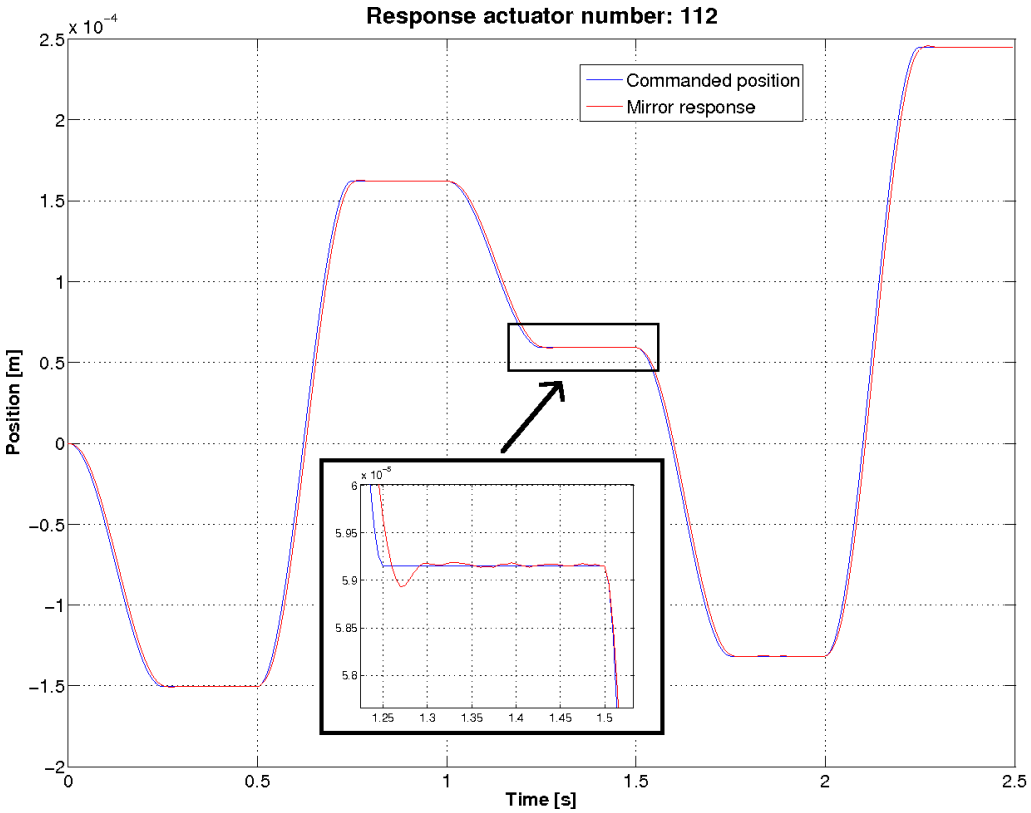

Figure 32: Rigid motions and mirror deformations together, simulation 5.

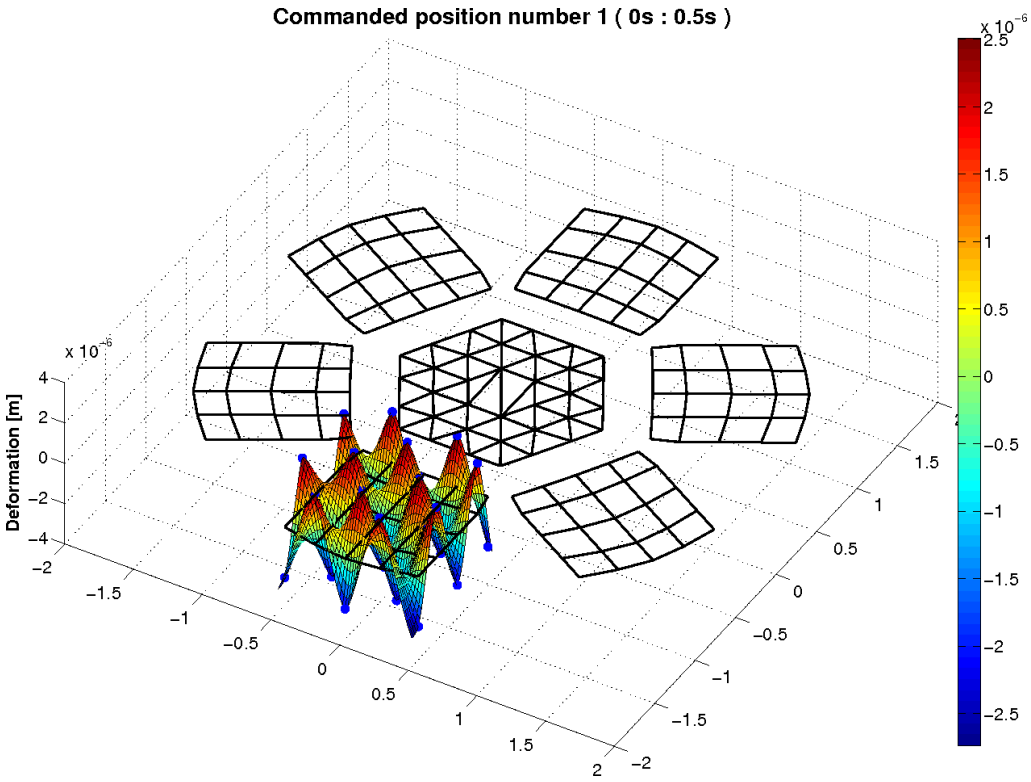

Figure 33: Chess square 3D deformation, simulation 6.

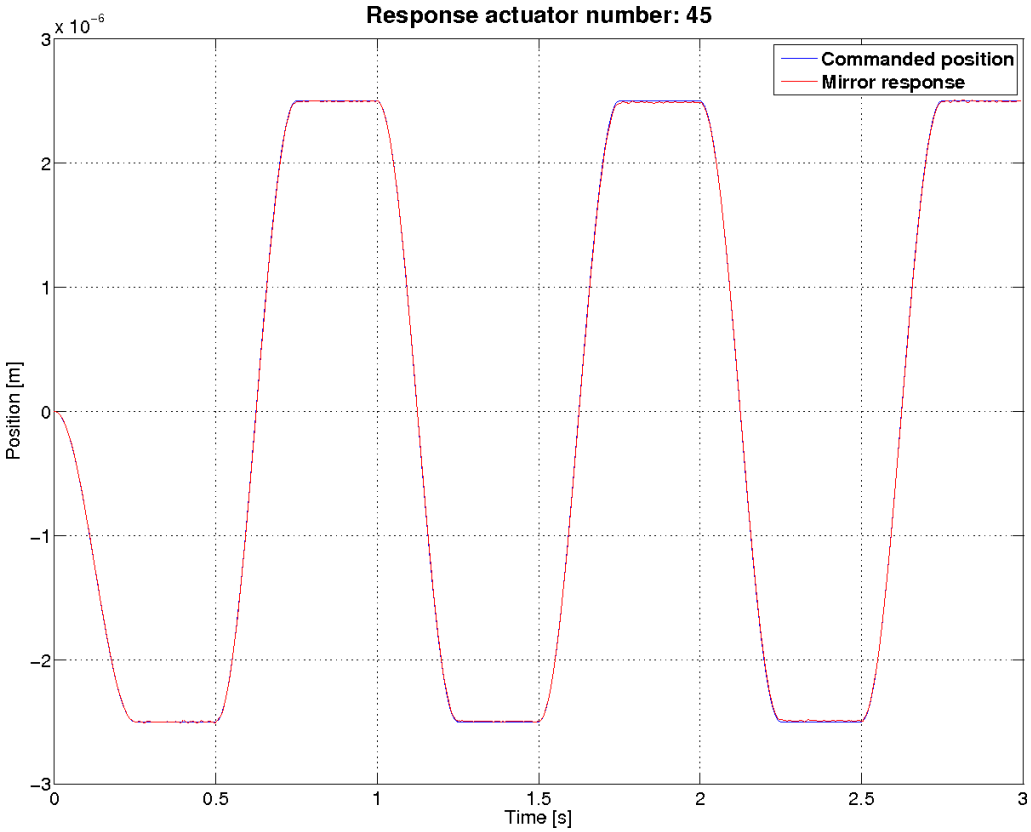

Figure 34: Simulation response of chess square petal deformation, simulation 6.

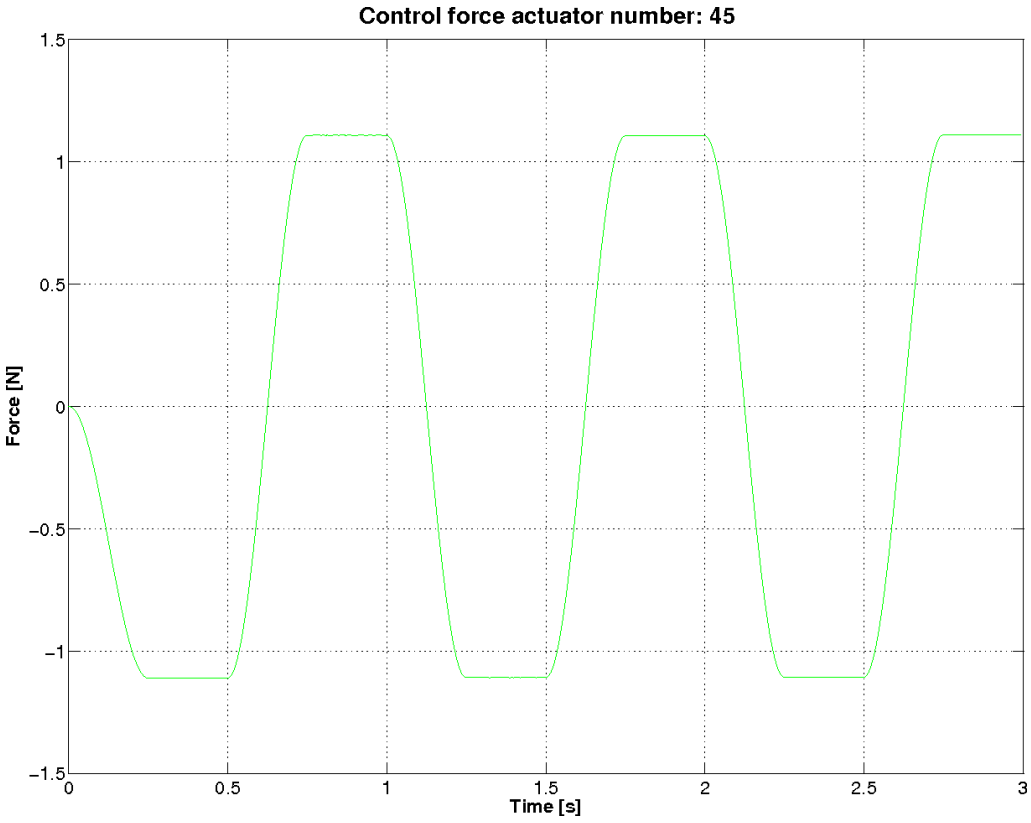

Figure 35: Force value needed to perform a chess square shape, simulation 6.

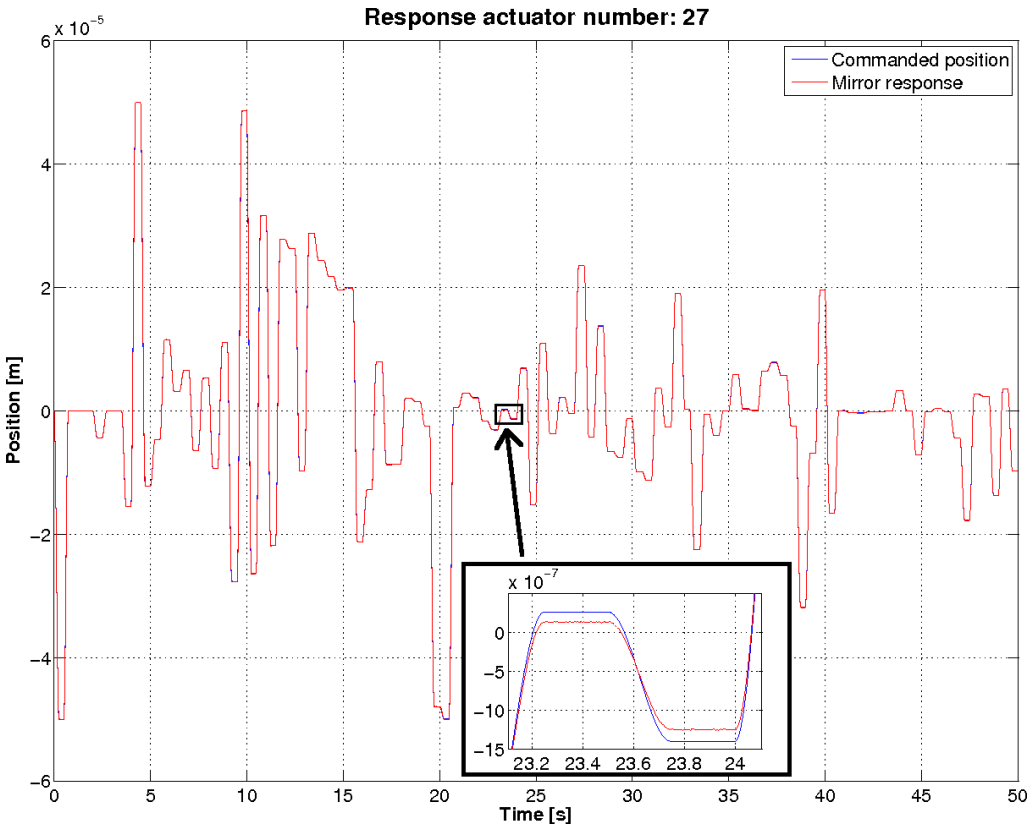

Figure 36: Mirror response to modal change commanded story, simulation 7.

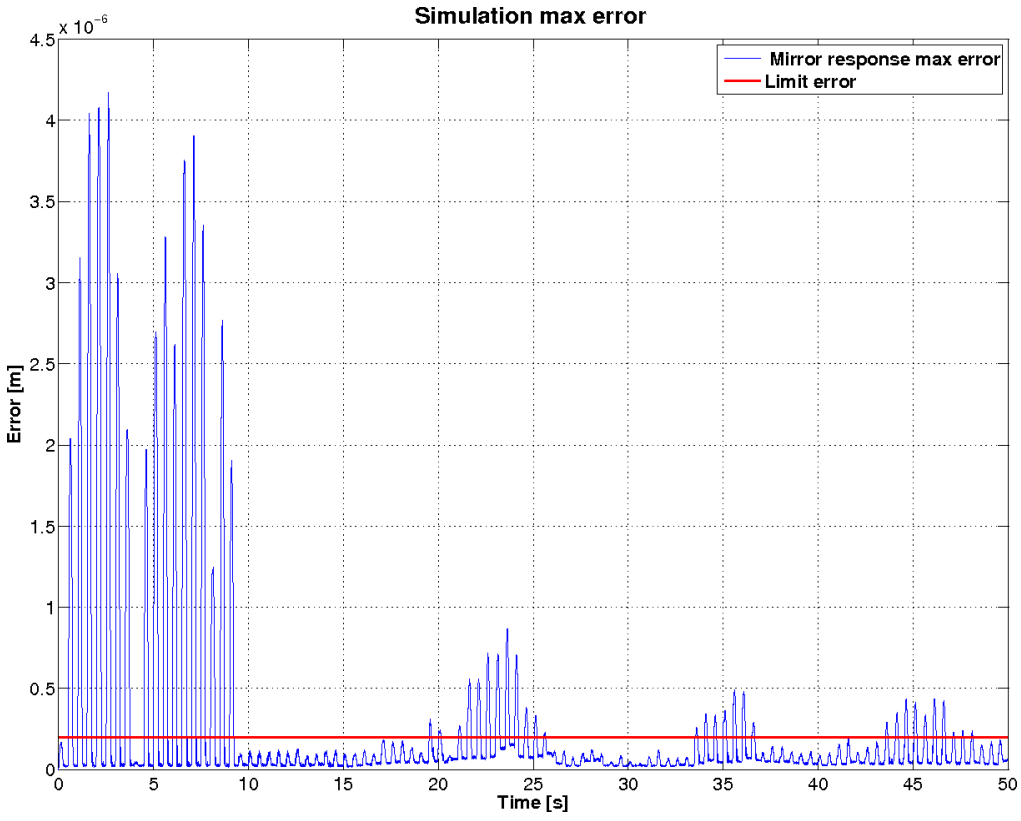

Figure 37: Mirror response maximum error, simulation 7.

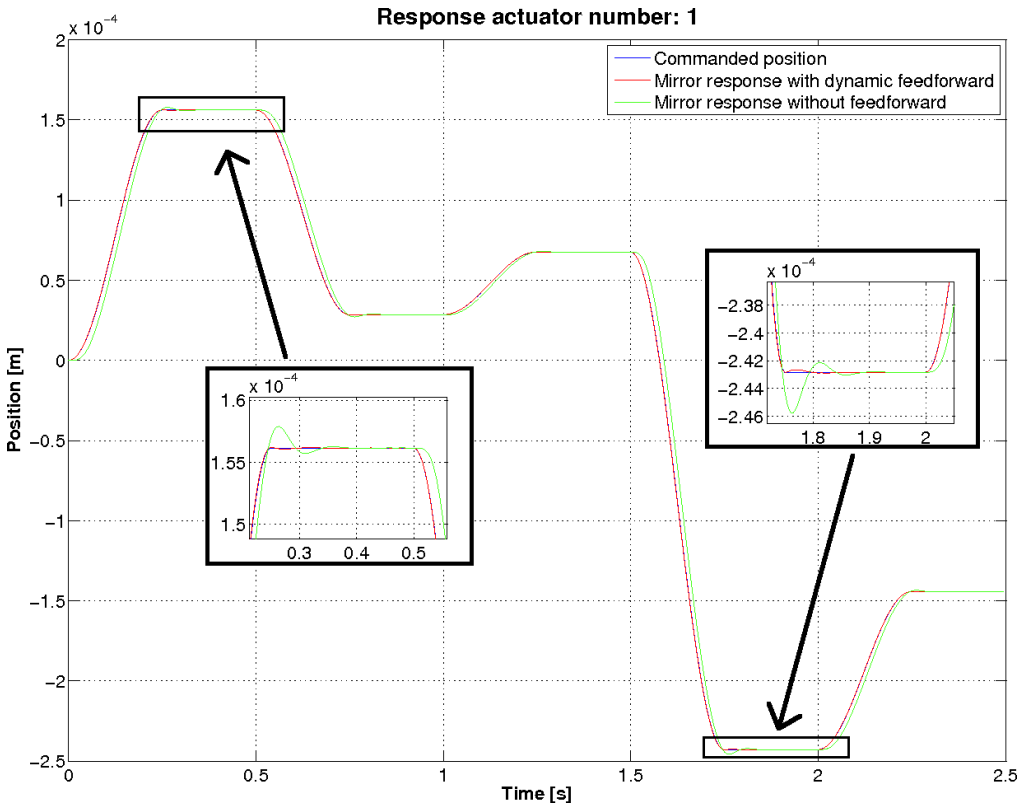

Figure 38: Comparison between response with and without dynamic feedforward contribution, simulation 8.

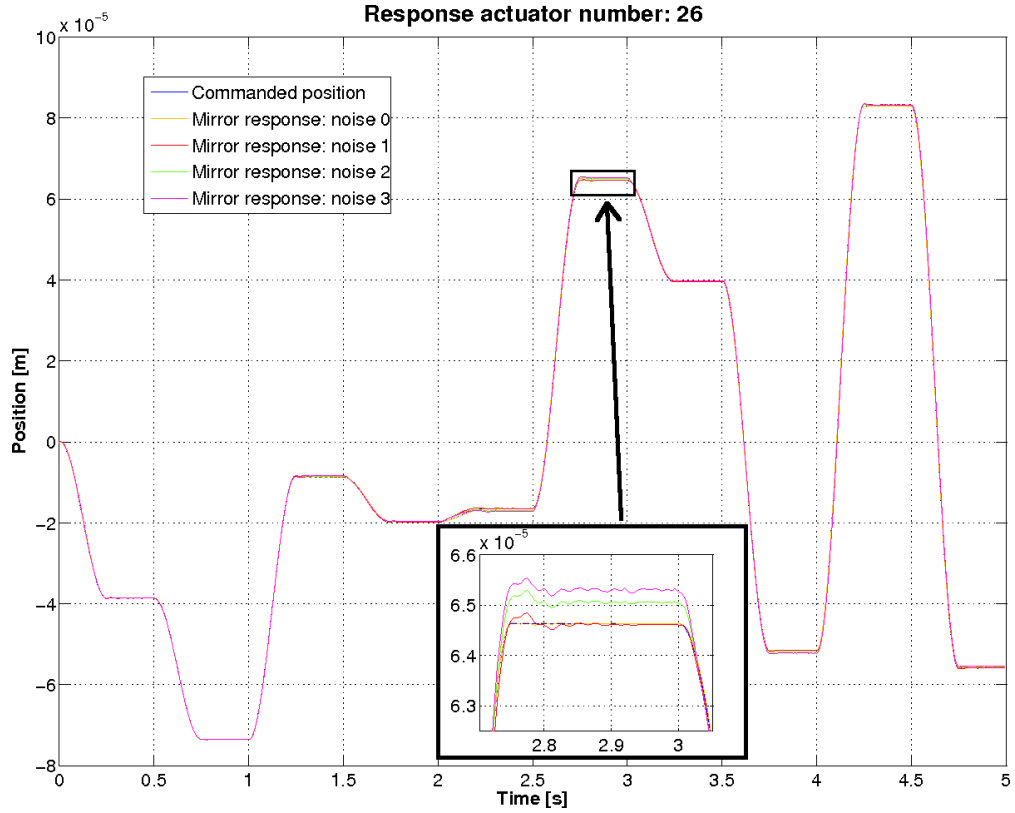

Figure 39: Comparison between responses with different identified stiffness matrices, simulation 9.

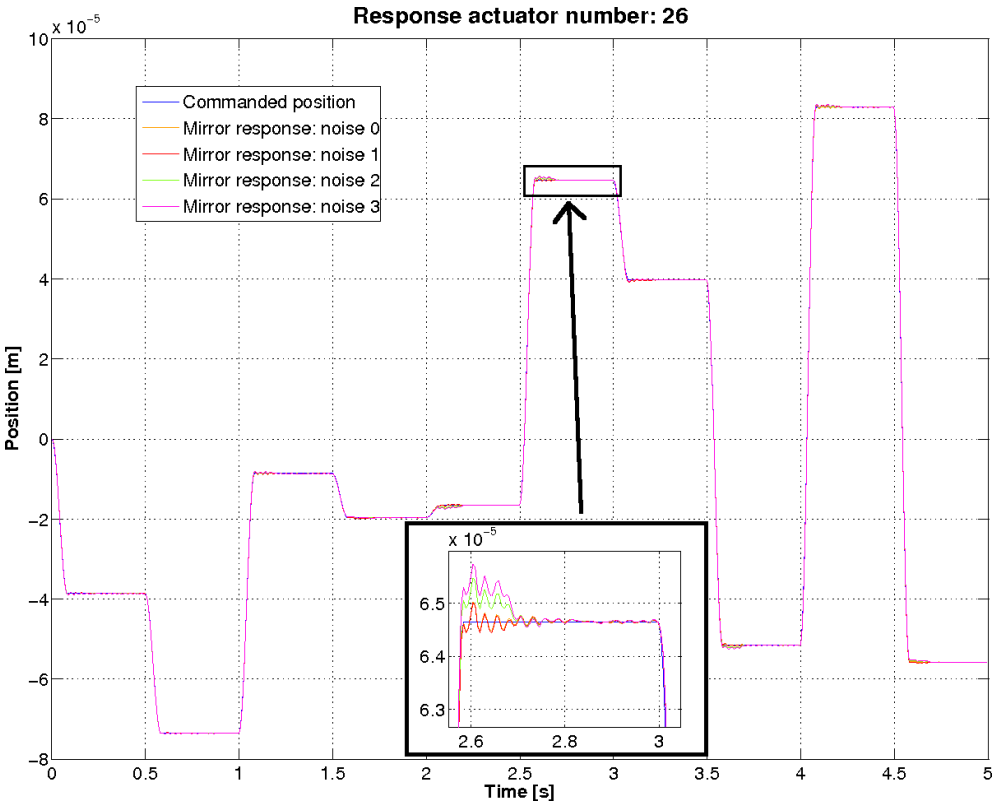

Figure 40: Comparison between responses with different identified stiffness matrices, using sub-stepping technique and 10 KHz control frequency, simulation 9.

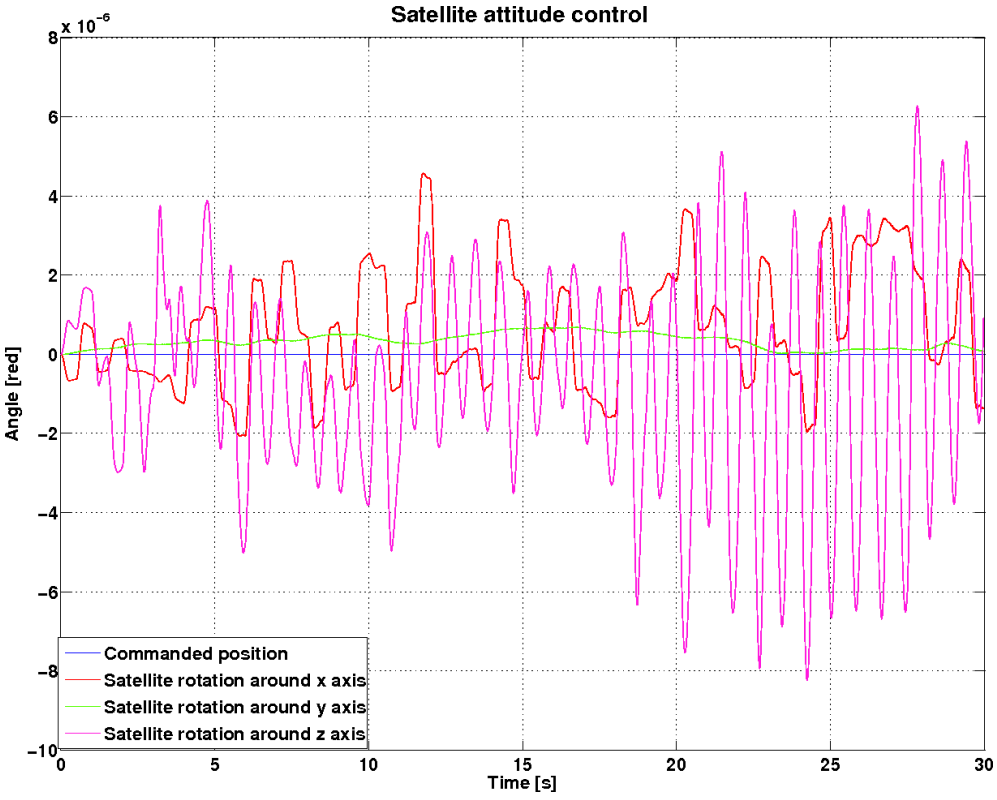

Figure 41: Satellite rigid rotations with null commanded angles.

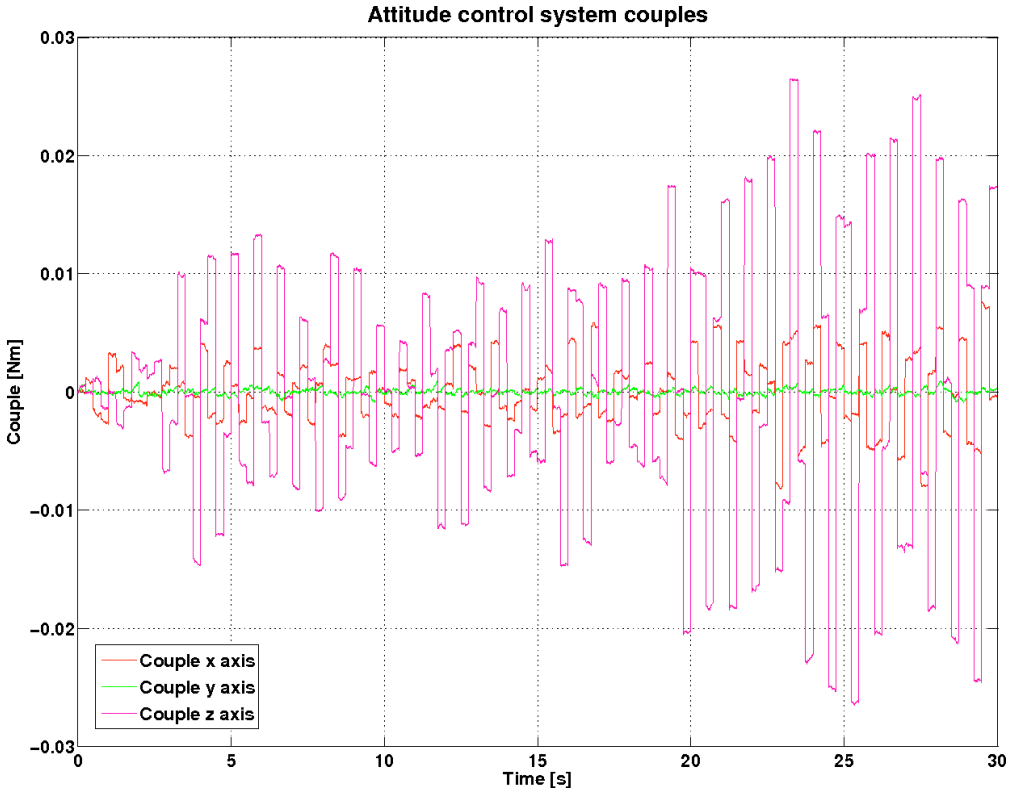

Figure 42: Satellite attitude couple needed to maintain the null angles position.

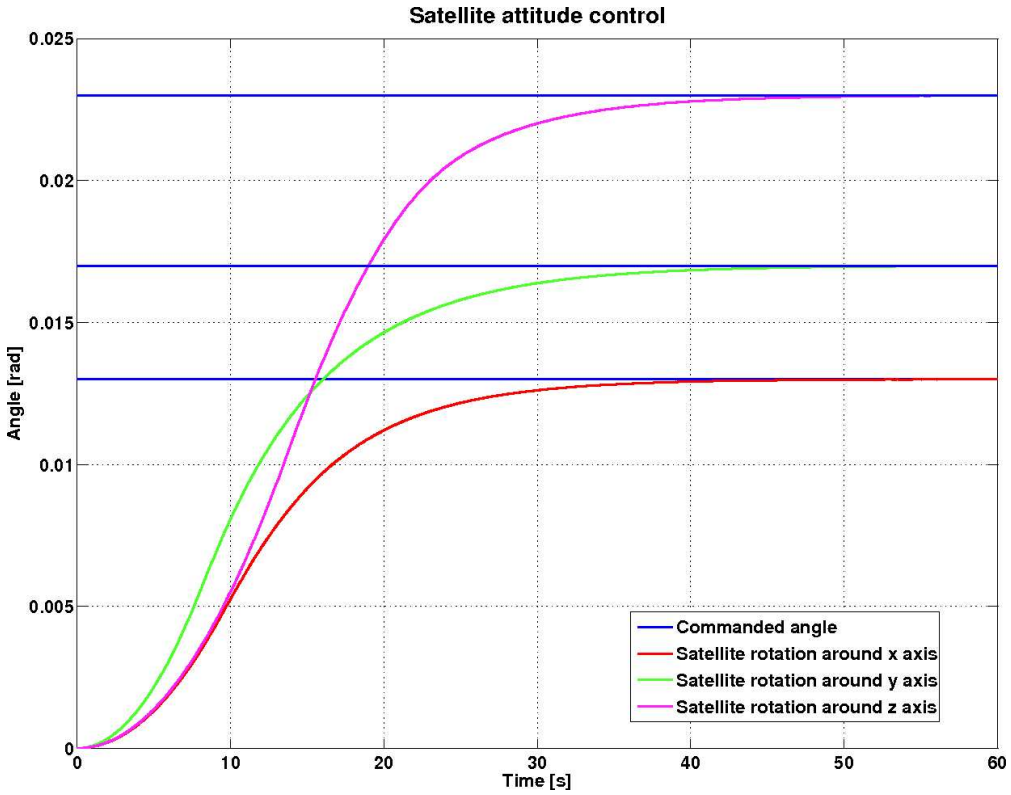

Figure 43: Satellite rigid rotations with non-null commanded angles.

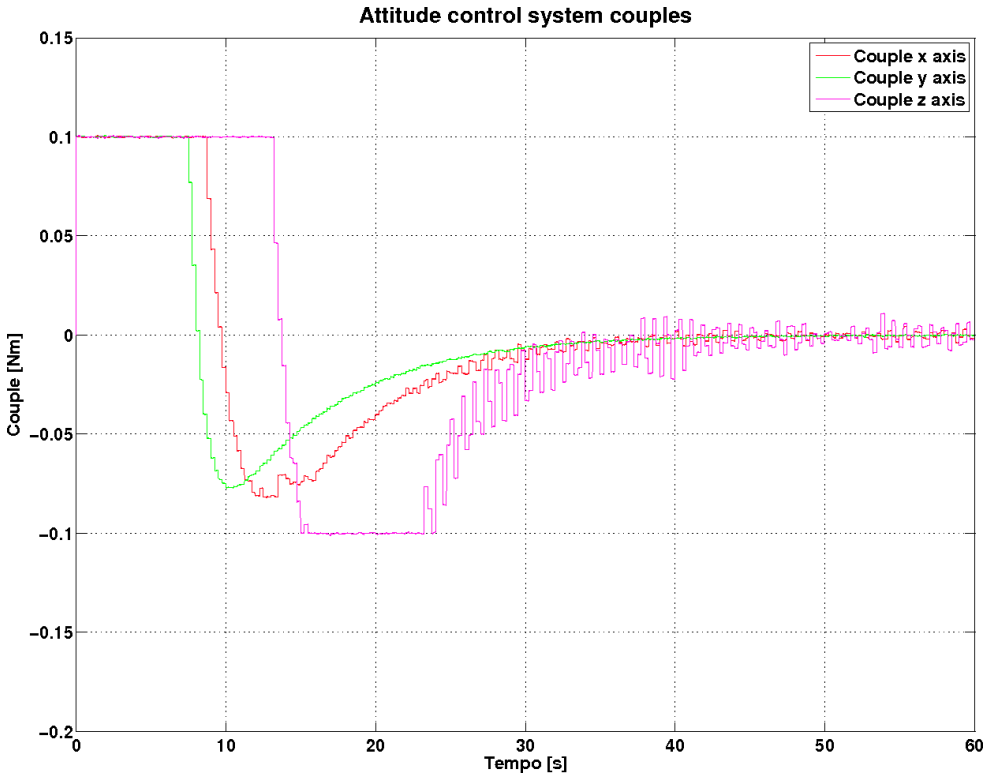

Figure 44: Satellite attitude couple needed to reach the commanded angles of rotation.

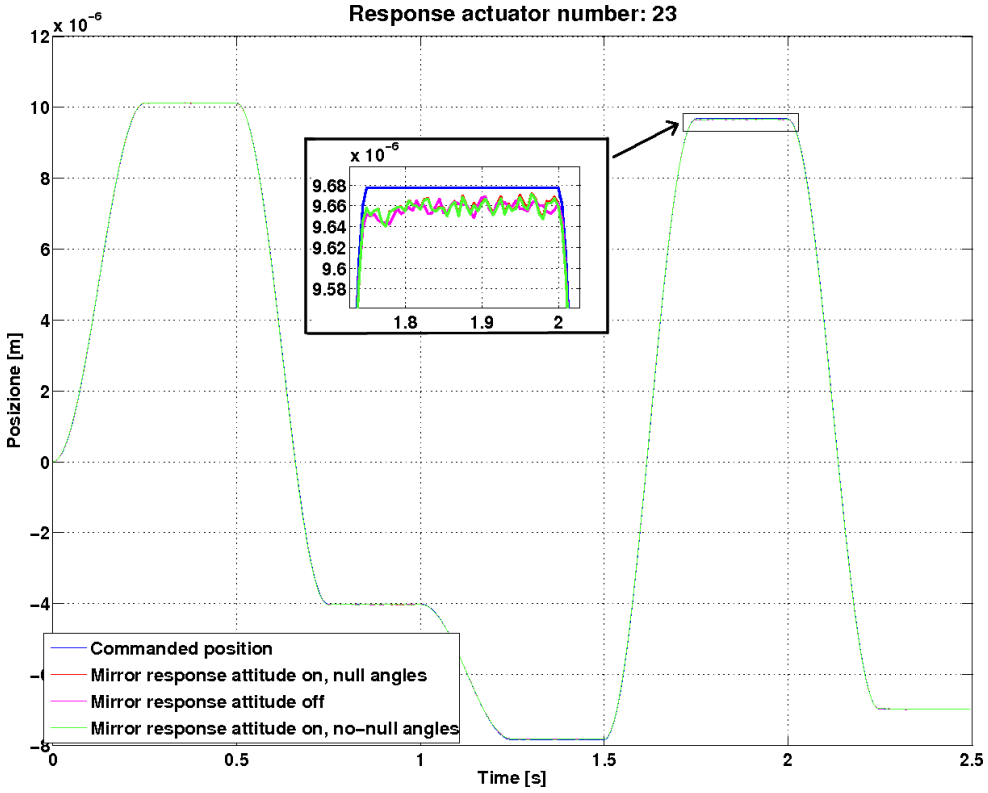

Figure 45: Comparison between responses performed with the attitude control system switched on and switched off.

12 Conclusions

The simulations carried out demonstrate that the mirror control system can satisfy the design specifications. In particular the controller allows the correct achievement of the final commanded positions with an acceptable precision. The performance is satisfactory both for small and high amplitude commanded motions/deformations. The capability to control rigid motions has been verified too, showing the controller effectiveness within a wide range of rigid displacements, ± 0.0005 m, and with elastic deformations coupled to rigid movements.

The most significant parameters limiting controller performances are the low structural damping and the constraint on the sampling frequency, that has to be keep as low as possible to limit power consumption. Moreover all the controller components that can add any delay are important to define the control system capabilities. Among them we must remark the importance of setting appropriate bandwidths for the first-order filters used to approximate the dynamics of sensors/actuators and the time derivatives. For that an appropriate compromise must be established to avoid high delays (low filters frequencies) and spillover (high filters frequencies). Another important delay can be introduced by acquisition/conversion (A/D/A) and computational delays. In this report as we have adopted a likely cautious solution by using half of the controller time step for the just mentioned delays. While negligibly affecting stability boundaries sensors and actuators noises, together with their quantization errors, are of paramount importance in determining control precision. Moreover the quantization introduces a nonlinear effect that produces positioning limit cycles through a sort of bang-bang control. So these phenomena have to be taken into account because they can affect both precision and stability of the controller. It has been underlined also that system noises and errors are highly significant in setting the achievable precision of the identified stiffness matrix. That is particularly important for the LIDAR project because the low passive damping available and the constraint of a low control frequency lead to poor dynamic control performances, while the sub-stepping technique cannot be used. So the final controller precision is mainly linked to a good stiffness identification. Fortunately it has been possible to demonstrate that with the actual system parameters a very good stiffness approximation can be identified.

It has been also verified that control forces can exceeds their saturation limit when large corrections have to be applied. This problem could be linked both to too widely random shape requests and to model uncertainties, in particular around the mirror-actuator hinged connections which add a significant stiffening effect that is difficult to correct especially on the petals. So a new verification should be performed when all the structural details and the controller capabilities approach their final design solution. However the simulations carried out so far have already demonstrated the need of a sufficiently stiff connection between the petals back-plates and the satellite central body.

From the control law point of view the results indicates the remarkable effectiveness of the solution based on a PD2 feedback term coupled to an appropriate open-loop feedforward aimed at canceling the modeled mirror dynamics as far as possible. It has been shown that the feedforward term can be profitably split into a static and a dynamic contribution, the first assuring a correct final steady position, the second improving the dynamic controller performances during the transient phase of the command tracking.

The simulation program takes advantage from a high frequency recovery through the static residualization technique, that allows to avoid inaccuracies in the estimation of the steady state controller forces linked to the use of the simpler truncated reduced modal base. Moreover the identification of the structural stiffness can be performed both with the real process simulation or with a simpler static determination of the final commanded position. We have shown that the results thus obtained are comparable and that the static response method allows to save a lot of

time, so greatly improving processing efficiency.

The simulations have demonstrated that the satellite attitude control system does not interfere significantly with the mirror controller, because they act mostly in an uncoupled mode.

The evaluations of the secondary mirror displacements due to the active mirror control activity have shown that without important rigid motions the magnitude of the misalignment of the line of sight with the image capture sensor is below 100 nm. The related boundary ranges grow up in presence of significant mirrors rigid motions, reaching maximum values of about 600 nm during the corresponding relatively large transients. Such a situation is mainly linked to the coupling between the first elastic petals modes, involving petals hinges stiffness, and the secondary mirror spike modes. So a possible solution could be to set a good frequency separation between these elements through an appropriate structural design. It is important to remark however that if the mirrors will not be required to large rigid correction motions, the secondary mirror displacements can be well contained in a range of about 20-30 nm.

The next step should be an improved update of the whole model in relation to the setting of integrated design specifications. Finally, once all the system parameters and the performance specifications are frozen and cleared, a final control system optimization might be possible in view of finding the lowest sampling frequency capable of ensuring the satisfaction of all the specifications with the least power consumption possible.